

Two-dimensional flow of foam around a circular obstacle: local measurements of elasticity, plasticity and flow

BENJAMIN DOLLET^{1,2} AND FRANÇOIS GRANER¹

¹Laboratoire de Spectrométrie Physique, BP 87, 38402 Saint-Martin-d'Hères Cedex, France

²Physics of Fluids, University of Twente, PO Box 217, 7500 AE Enschede, The Netherlands

(Received 15 May 2006 and in revised form 20 March 2007)

We investigate the two-dimensional flow of a liquid foam around a circular obstacle by measuring all the local fields necessary to describe this flow: velocity, pressure, and bubble deformations and rearrangements. We show how our experimental set-up, a quasi-two-dimensional ‘liquid pool’ system, is adapted to the determination of these fields: the velocity and bubble deformations are easy to measure from two-dimensional movies, and the pressure can be measured by exploiting a specific feature of this system, a two-dimensional effective compressibility. To describe accurately neighbour swapping (so-called ‘T1’ processes), we propose a new, tensorial descriptor. All these quantities are evaluated via an averaging procedure that we justify by showing that the fluctuations of the fields are essentially Gaussian. The flow is extensively studied in a reference experimental case; the velocity presents an overshoot in the wake of the obstacle, and the pressure is maximum at the leading side and minimal at the trailing side. The study of the elastic deformations and of the velocity gradients shows that the transition between plug flow and yielded regions is smooth. Our tensorial description of T1s highlights their correlation both with the bubble deformations and the velocity gradients. A salient feature of the flow, notably for the velocity and T1 distribution, is a marked fore–aft asymmetry, the signature of the elastic behaviour of the foam. We show that the results do not change qualitatively when various control parameters (flow rate, bubble area, fluid fraction, bulk viscosity, obstacle size and boundary conditions) vary, identifying a robust quasi-static regime. These results are discussed in the framework of the foam rheology literature. A movie is available with the online version of the paper.

1. Introduction

Liquid foams have a ubiquitous mechanical behaviour: depending on the strength of an external applied perturbation, they can exhibit simultaneously an elastic, plastic and viscous response (Weaire & Hutzler 1999; Höhler & Cohen-Addad 2005). This complex behaviour is used in many industrial applications (Khan & Prud'homme 1996), such as ore flotation, oil extraction, and the food and cosmetic industry. Liquid foams are also of fundamental interest as models for studying complex fluids, since their constituent, bubbles, are experimentally easily observable, unlike colloids or polymers. The need to understand of foam rheology has motivated research; a series of seminal studies has first focused on the elastic properties of foams, such as elastic moduli or yield stress (Derjaguin 1933; Princen 1983; Stamenović & Wilson 1984; Khan & Armstrong 1986). The plasticity of foams originates from topological rearrangements, called T1s (figure 2*c*, below). This coupling between local rearrangements

of constitutive entities and a macroscopic plastic behaviour is a general feature of many materials (emulsions, pastes, slurries), that have been described generically as soft glassy materials (Sollich *et al.* 1997). Viscous dissipation in foams has also been studied for more than two decades (Kraynik 1988 and references therein; Buzza, Lu & Cates 1995; Gopal & Durian 2003; Cohen-Addad, Höhler & Khidas 2004), with a recent interest in describing friction between bubbles and walls (Kern *et al.* 2004; Denkov *et al.* 2005; Cantat & Delannay 2005; Dollet *et al.* 2005b).

Much effort is currently being devoted to integrating elastic, plastic and viscous behaviours into a single constitutive equation (Höhler & Cohen-Addad 2005; Janiaud, Weaire & Hutzler 2006). To achieve such a goal, a precise knowledge of the mechanical behaviour of the foam is required. This is why foams are often studied in quasi-two-dimensional geometries (Cox, Vaz & Weaire 2003; Vaz & Cox 2005), where foams are confined so that they are only one bubble thick (confinement between two parallel plates, between one horizontal plate and the surface of a soap solution, or at the free surface of a soap solution). Imaging is easier in these quasi-two-dimensional geometries than in to an opaque three-dimensional foam. A classical way to study quasi-two-dimensional foams is to use rheometric flows (Larson 1999), like simple shear flows (Wang, Krishan & Dennin 2006) or cylindrical Couette geometries (Debrégeas, Tabuteau & di Meglio 2001; Lauridsen, Twardos & Dennin 2002), which are easy to analyse. The study of heterogeneous flows is complementary: they are less easy to analyse and to understand, but the variety of observed effects is larger. This is the case for example for flows in constrictions (Asipauskas *et al.* 2003), or for Stokes experiments, i.e. flows around obstacles (Cox *et al.* 2000; de Bruyn 2004; Dollet *et al.* 2005a; Cantat & Pitois 2005; Dollet, Aubouy & Graner 2005a; Dollet, Durth & Graner 2006).

We have studied extensively Stokes experiments for foams, focusing on the effect of the foam on the obstacle: drag (Dollet *et al.* 2005c), lift (Dollet *et al.* 2005a) and torque (Dollet *et al.* 2006). The variations of these quantities with various control parameters, especially the foam flow rate, illustrate the interplay between elastic, plastic and viscous behaviour of the foam. To go beyond these force and torque measurements, here we revisit some of these experiments with a complementary approach: studying using local measurements the effect of the presence of an obstacle on a flowing foam. We present a method developed to analyse precisely and completely this local response, quantified by various local fields. We extract velocity and velocity gradients, bubble deformations, and pressure, which describe the elastic and viscous parts of the foam response. We also define a new tensorial descriptor of the bubble rearrangements, and present the corresponding field, which quantifies accurately the foam plastic response. The results highlight the differences between the foam local response and simple viscoplastic and viscoelastic responses. On one hand, the flow presented a marked fore–aft asymmetry, which is not captured by simple viscoplastic models. On the other hand, we identify regions where the foam yields and experiences a plastic flow, for which the mechanical load exerted by velocity gradients is compensated by stress relaxations associated with T1s. Our results thus motivate modeling coupling elastic, plastic and fluid behaviour, and they also constitute an extensive database to test and constrain such models.

2. Materials and methods

2.1. Experiment

We perform a Stokes experiment (de Bruyn 2004; Dollet *et al.* 2005c; Cox *et al.* 2000; Asipauskas *et al.* 2003), i.e. we study the flow of foam around obstacles (figure 1),

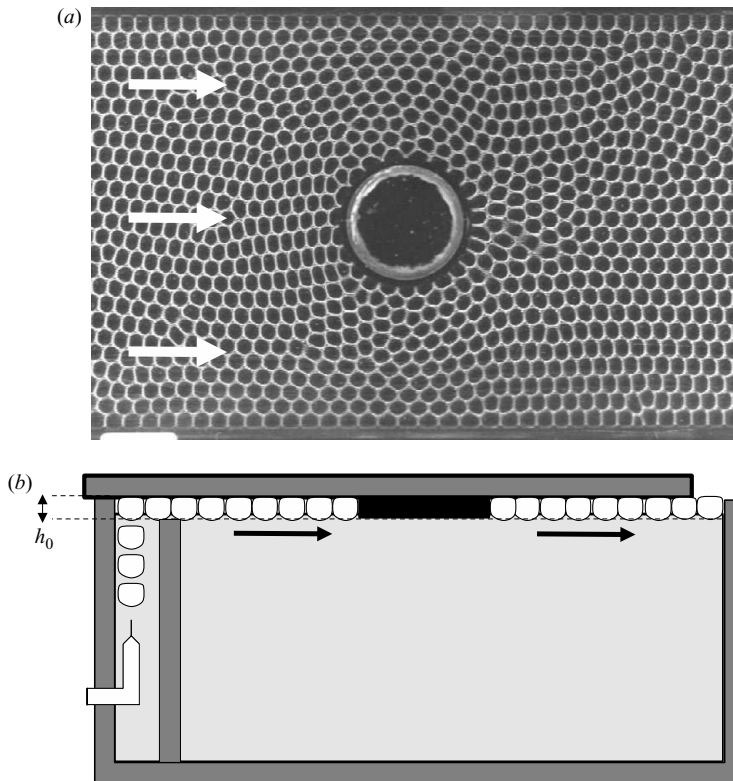


FIGURE 1. (a) A photograph of foam flowing from left to right (arrows) around a circular obstacle of diameter 30 mm. The bubble size is 16.0 mm^2 (note the monodispersity of the foam), and the flow rate is 176 ml min^{-1} . The walls of the channel (width 10 cm) are visible at the top and bottom of the picture. The surface of the observed field is $15.4 \times 10.2\text{ cm}^2$. A movie is available with the online version of the paper. (b) Side view of the set-up. The foam is constituted by a monolayer of bubbles and the black rectangle represents the obstacle.

using a foam channel fully described in Dollet *et al.* (2005c). Briefly, a tank is filled with a bulk solution obtained by adding 1% of commercial dish-washing liquid (Taci, Henkel) to desionized water. Its surface tension, measured with the oscillating bubble method, is $\gamma = 26.1 \pm 0.2\text{ mN m}^{-1}$, and its kinematic viscosity, measured with a capillary viscosimeter, is $1.06 \pm 0.04\text{ mm}^2\text{ s}^{-1}$ unless explicitly stated otherwise. Nitrogen is blown into the solution through a nozzle or a tube at a computer-controlled flow rate. This generates a ‘liquid pool foam’ foam (Vaz & Cox 2005), constituted by a horizontal monolayer of monodisperse bubbles (the polydispersity, measured as the relative width of the bubble area distribution, is less than 3%) of average thickness h_0 , confined between the bulk solution and a glass top plate. This is a quasi-two-dimensional foam (Cox *et al.* 2003; Vaz & Cox 2005): despite the three-dimensional geometry of the bubbles (figure 1b), it undergoes a two-dimensional horizontal flow. Moreover, there is an equilibrium between the water in the bulk solution and in the films separating bubbles; the equilibration is much quicker than the transit of the bubbles to the obstacle, hence the effect of drainage is minimized. Two other quasi-two-dimensional foams exist: the bubble raft (no confinement), and the Hele-Shaw cell (confinement between two horizontal plates). Unlike these two

systems, the liquid pool foam has an effective in-plane compressibility (Dollet *et al.* 2005c), which enables pressure to be measured easily, as described in §2.3.1. The fluid fraction is adjusted by changing the foam thickness (Raufaste *et al.* 2007). The foam flows around an obstacle placed in the middle of the channel; we choose the flow rate between 24 and 515 ml min⁻¹ (corresponding velocities: 0.11 to 2.5 cm s⁻¹). We will study a reference case characterized by the following values of the parameters: circular obstacle of diameter 30 mm, flow rate of 176 ml min⁻¹, bubble area of 16.0 mm², foam thickness of 3.5 mm (fluid fraction 4.3%), and bulk viscosity of 1.06 mm² s⁻¹. We will study the influence of each control parameter separately.

This set-up allows us to measure forces on obstacles (Dollet *et al.* 2005a, c) and pressure drops associated with the flow of foam (Dollet *et al.* 2005b). For every experiment we record 750 images, representing a movie of 30 s. From these movies, we extract all relevant quantities describing the flow of foams: velocity, pressure, elastic stress, bubble deformations, and bubble swapping (topological rearrangements, or T1s) using a procedure that we developed, as follows.

2.2. Image analysis

2.2.1. Skeletonization of experimental images

With the NIH Image software, we invert the grey levels of the images, then threshold them, to clearly separate the black network of edges from white bubbles. We have defined several zones on the image, each with different thresholds, to compensate for slight remaining spatial variations of light intensity. We then extract the network of bubble edges from the experimental images by a classical skeletonization procedure, which reduces the foam to a network of one-pixel-thick edges (figure 2a).

This procedure conserves the topology between the real and the skeletonized bubbles (figures 1a and 2b), which enables a proper evaluation of the bubble deformation, as explained in §2.3.3. It has two limitations: first, it distorts the geometry and curvature of the bubbles edges and vertices, which prevents us from precisely evaluating the elastic stress, since this requires integration along all edges (Batchelor 1970). Second, it is not adapted to the boundaries; we therefore systematically eliminate the data near the obstacle and the channel walls.

2.2.2. Treatment of skeletonized images

For a two-dimensional skeletonized foam, the bubbles are bounded by thin edges, which merge in threefold vertices. Bubbles are thus easily labelled, and a vertex can be unambiguously defined as a black pixel for which, among its eight neighbouring pixels, one can find three pixels belonging to three different bubbles. Boundary vertices are defined as pixels on boundaries, with two neighbouring pixels belonging to two different bubbles.

We scan an image in two steps. In a first step, each individual bubble is labelled with a given number. The program records a list of bubbles, each bubble being represented by its number b , its number of pixels N_b , and the position \mathbf{x}_b of its centre of mass. In a second step, vertices are identified and labelled, and the program records them in a second list, each vertex being represented by its number, its coordinates and the labels of its neighboring bubbles. The subsequent analysis does not require the image.

To compute the fields, we mesh the image by a rectangular grid. We have checked that there exists a range of mesh sizes for which the results do not change (figure 3): this validates our choice, and is a first indication of the continuous character of the foam (see §3.1). We have chosen to mesh the image with a rectangular grid of 26×17 (nearly) square boxes of side 6 mm: such a choice enables us to capture well the

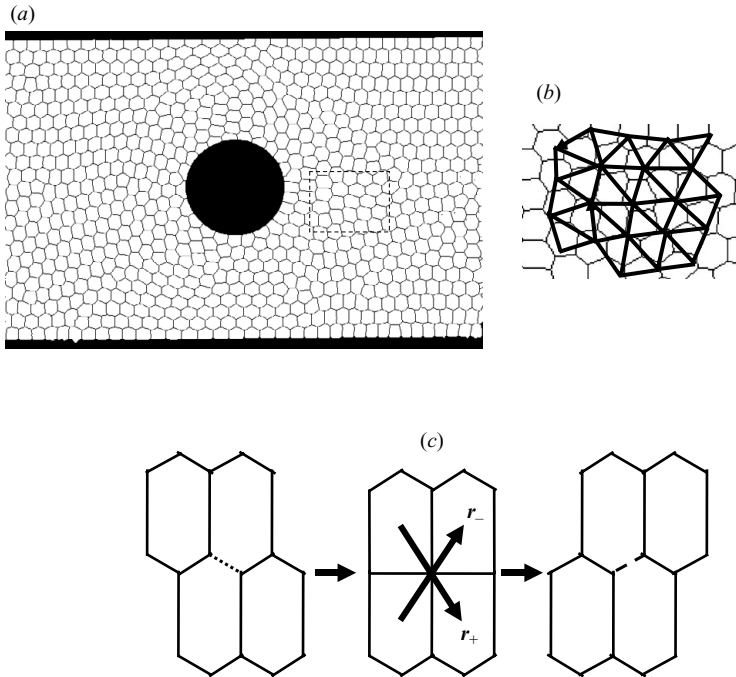


FIGURE 2. (a) Skeletonized image of foam. (b) Enlargement of the zone framed by the dashed rectangle in (a): the network of bubble edges is shown with thin lines, and the (triangular) centre network with thick lines. (c) Sketch of a side-swapping event (topological rearrangement, also called a T1 event). Left: the edge to disappear is dotted; middle: definition of the vectors r_+ and r_- ; right: the new edge is dashed.

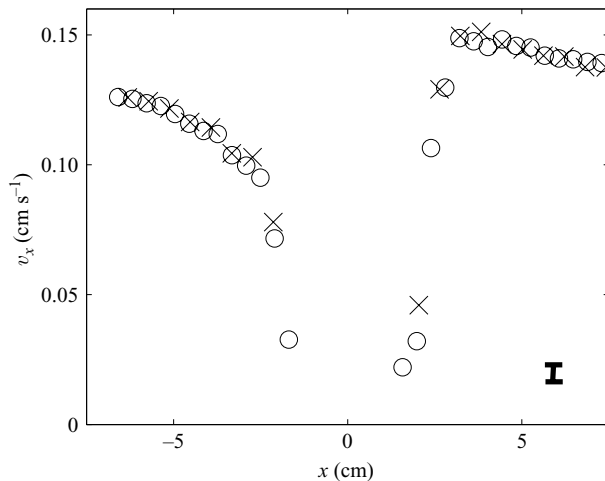


FIGURE 3. Plot of the velocity v_x along the axis of symmetry of the flow, as a function of the streamwise coordinate x , for a flow rate of 24 ml min^{-1} and for two mesh sizes (\times : boxes of area $6.0 \times 6.2 \text{ mm}^2$, \circ : boxes of area $4.1 \times 4.1 \text{ mm}^2$). The error bar at the bottom right of the plot is estimated from the statistical dispersion of the data at $\pm 3 \times 10^{-3} \text{ cm s}^{-1}$, i.e. 2% of the average velocity.

variations at the macroscopic scale, and the statistics is sufficient for these variations to be smooth (during the whole movie, about 2×10^3 bubbles are computed per box). Each bubble is attributed to the box in which its centre lies.

2.2.3. Direct measurements from skeletonized images

From the list of bubbles, we compute the network of the vectors \mathbf{r} linking the two centres of bubbles in contact, which we call the centre network (figure 2b). To be precise, each vector \mathbf{r} is attributed to the two boxes (with a coefficient 1/2 each) of the two bubble centres it binds. We then compute the texture tensor (Aubouy *et al.* 2003):

$$\mathbf{M} = \langle \mathbf{r} \otimes \mathbf{r} \rangle, \quad (2.1)$$

which is the second-order tensor of components: $M_{ij} = \langle r_i r_j \rangle$. The average is performed over 750 images and all vectors in the box. This tensorial quantity has proved to be a good descriptor of bubble deformation: it reproduces the size, direction and amplitude of deformation of bubbles in studies where it has been computed over the bubble edges network ℓ (Asipauskas *et al.* 2003; Courty *et al.* 2003; Janiaud & Graner 2005). Here, we calculate it over the centre network, making it much more general: it applies to three-dimensional foams, and to wet foams such as the ones considered herein. It is also more robust, because the centres of mass, hence the vectors \mathbf{r} , are much less biased by skeletonization than the bubble edges. However, the two possible network choices are equivalent at low bubble deformation, where they give the correct expression for the shear modulus of the foam (Dollet).

In order to compute the velocity field, we compare successive frames. In the range of flow rates studied, the displacement of a bubble between two successive frames is small compared to its size; the displacement of the bubble centres is thus easy to calculate, and we average all displacements in each box to get the velocity field (an Eulerian rather than Lagrangian point of view).

The detection of the T1s is also based on the correlation of two successive images; a T1 is a topological neighbour-swapping event, during which a bubble edge disappears and a new one is created (figure 2c). The program tracks independently the disappearing and appearing edges, by comparing the list of edges of two successive frames. This decoupling of the disappearing and appearing edges is necessary for two reasons: first, the duration of a T1 event is sometimes longer than the time interval between two successive frames (0.04 s); second, the transient fourfold vertex (middle of figure 2c) contains a certain amount of liquid. After skeletonization, this is often erroneously recognized as an artificial small four-sided bubble between the four bubbles experiencing the T1, which we remove by imposing a lower threshold on the bubble area. A T1 covers two distinct instantaneous events: one disappearance and one appearance of a link between two bubbles. To a disappearing (appearing) edge is associated the vector of the centre network \mathbf{r}_- (\mathbf{r}_+) which links the centres of the two separating (attaching) bubbles. A complete quantification of T1s, including not only their frequency but also their direction, must rely on these vectors, whose direction is irrelevant by definition. We thus define the tensor $\mathbf{T}_\pm = f_\pm \langle \mathbf{r}_\pm \otimes \mathbf{r}_\pm \rangle$, where f_- (f_+) is the frequency of separation (attachment) events per link \mathbf{r} of the centre network. In this paper, we use an alternative definition, based on unit vectors: $\mathbf{T}_\pm^{\text{adim}} = f_\pm \langle \hat{\mathbf{r}}_\pm \otimes \hat{\mathbf{r}}_\pm \rangle$, which has the advantage of being directly proportional to the frequency of T1s.

2.3. Computation of the fields

We present here the relevant fields describing the flow of foams, and the way in which they are computed from the image analysis detailed in the previous section.

2.3.1. Pressure

As already mentioned in Dollet *et al.* (2005c), in a quasi-two-dimensional set-up with foam confined between a top plate and a liquid pool, the depth of bubbles adjusts to pressure variations. The three-dimensional compressibility of the bubbles

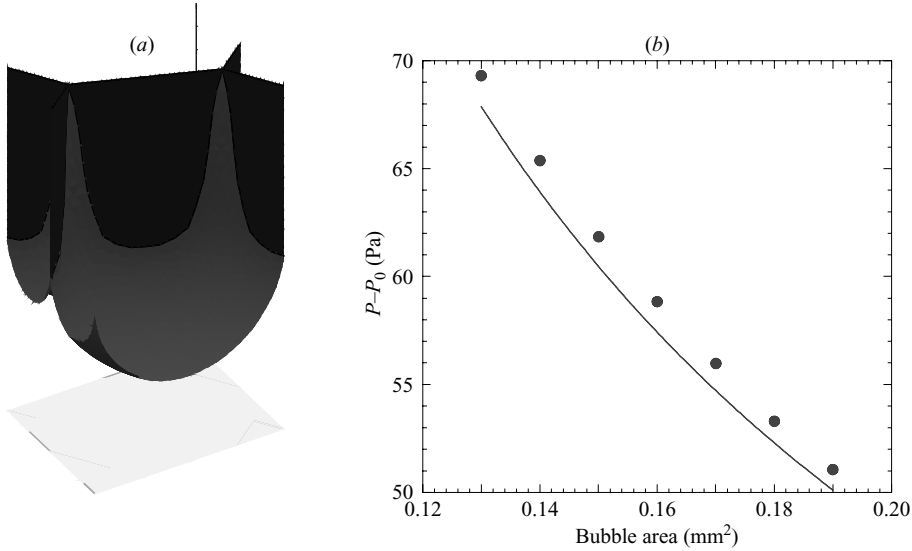


FIGURE 4. (a) Shape of a bubble of area 16.0mm^2 , and of volume $\mathcal{V} = 16.0 \times 3.5\text{mm}^3$, calculated by Simon Cox with the Surface Evolver. To fit to the experimental situation, both hexagonal symmetry and buoyancy are input in the computation; as an only simplifying assumption, the junction between lateral faces and the top plate is assumed orthogonal. (b) Pressure difference $P - P_0$ as a function of the bubble area. The dots are from the calculations with the Surface Evolver, and the curve is from (2.2), without free parameters.

is negligible here: for an ideal, isothermal gas, the compression modulus is of order 10^5Pa , which is four orders of magnitude higher than the measured local variations of pressure, as shown later (figure 12). Hence, the volume of a given bubble is constant. Therefore, the horizontal bubble area varies with its pressure: the foam thus has an effective two-dimensional compressibility in the plane of the top plate.

To obtain an accurate relation between area and pressure variations, we refine our earlier estimate (Dollet *et al.* 2005c). On the time scales of the flow, the pressure P is constant in the bubble, and at the bottom of the bubble can be written: $P = P_0(x) + \rho gh + \gamma\mathcal{C}$, where P_0 is a reference pressure, ρ the volumetric mass of the solution, h the depth of the bubble and \mathcal{C} its curvature at the bottom. Note that the reference pressure takes into account the pressure drop along the channel (Dollet *et al.* 2005b). The shape of the bubble is quite complex (figure 4a); to simplify, we assume its bottom has the shape of a truncated sphere of radius a related to the bubble area: $A = \pi a^2$. Hence, $\mathcal{C} \approx 2\sqrt{\pi/A}$. Writing $\mathcal{V} \approx Ah$ for the (constant) volume of the bubble, we obtain the following relation between area and pressure:

$$P - P_0(x) = \frac{\rho g \mathcal{V}}{A} + 2\gamma \sqrt{\frac{\pi}{A}}, \quad (2.2)$$

with $\rho = 10^3\text{kg m}^{-3}$ the volumetric mass of the solution, $g = 9.8\text{m s}^{-2}$ the gravitational acceleration, and \mathcal{V} the constant bubble volume. The average bubble area is easily computed in each box with the image analysis program. Since the pressure field is scalar, it is as convenient to represent it as grey levels.

To validate our approximate evaluation, we compared it to the more realistic shape of a bubble computed with the Surface Evolver software (Brakke 1992) and represented in figure 4(a). Starting from a bubble of fixed volume $\mathcal{V} = 16.0 \times 3.5\text{mm}^3$, corresponding to our reference area and thickness, we compare the pressure computed

from (2.2) and from the Surface Evolver (figure 4b). The gap between the computations is only 2%, which validates our simple evaluation of the pressure. From (2.2), we evaluate the in-plane compressibility as $K = -A\partial P/\partial A = \rho gh + \gamma\sqrt{\pi/A} = 46 \text{ Pa}$ for our reference values $h = 3.5 \text{ mm}$ and $A = 16.0 \text{ mm}^2$, which is more than three orders of magnitude smaller than the gas compressibility.

2.3.2. Velocity and velocity gradients

The image analysis program provides the velocity field directly, which we represent as usual with arrows. The velocity gradient is computed by finite differences; we evaluate this gradient in the middle of the four boxes (i, j) , $(i, j + 1)$, $(i + 1, j)$ and $(i + 1, j + 1)$. We use the symmetric velocity gradient, the deformation rate: $\mathbf{D} = (\nabla\mathbf{v} + {}^t\nabla\mathbf{v})/2$, and the antisymmetric velocity gradient, the vorticity, which is a scalar for two-dimensional flows: $\omega = (\partial v_y/\partial x - \partial v_x/\partial y)/2$. We will explain how we plot the deformation rate, and the other tensorial quantities in §2.3.3. We will also use the scalar dissipation function (Guyon, Hulin & Petit 2001), defined as

$$\|\mathbf{D}\| = \sqrt{D_{xx}^2 + 2D_{xy}^2 + D_{yy}^2}, \quad (2.3)$$

which is a scalar measure of the amplitude of the velocity gradient.

2.3.3. Tensorial fields: texture, statistical elastic strain, $T1$

As stated in §2.2.2, we use the texture tensor as a descriptor of bubble deformations. To be more quantitative, we will use the statistical elastic strain tensor, defined as (Aubouy *et al.* 2003):

$$\mathbf{U} = \frac{1}{2}(\ln \mathbf{M} - \ln \mathbf{M}_0), \quad (2.4)$$

where \mathbf{M}_0 is a reference value, that we choose to be isotropic: $\mathbf{M}_0 = \lambda_0 \mathbf{I}$. Here, λ_0 is the average of the eigenvalues of the texture tensors evaluated at the upstream and downstream extremities of the observation field (left and right on figure 1), where the bubbles are less perturbed by the presence of the obstacle, and \mathbf{I} is the two-dimensional identity tensor. We have $\lambda_0 = r_0^2/2$, with r_0 the average length of a link between two bubble centres. For a hexagonal network, $r_0 = \sqrt{2A/\sqrt{3}}$, hence $\lambda_0 = A/\sqrt{3}$.

We use the statistical elastic strain tensor because it quantifies the elastic strain in foams with a wide generality. At small deformations, it coincides very closely with the classical elastic strain (Landau & Lifshitz 1981), and it extends it at large deformations (Asipauskas *et al.* 2003; Courty *et al.* 2003; Janiaud & Graner 2005). The precision of the statistical strain tensor as a measure of the elastic strain is estimated as 2%, from previous comparisons of the shear modulus of foams estimated with the statistical strain and independently measured (Courty *et al.* 2003) or calculated (Asipauskas *et al.* 2003). Furthermore, the statistical strain is also well-defined in flow situations, where nonlinear elastic descriptions of foams accounting for large deformations (Höhler, Cohen-Addad & Labiausse 2004) do not hold.

The trace of the statistical elastic strain tensor quantifies the relative variation of the area of the bubbles, which remains lower than 10% (Dollet *et al.* 2005c); hence, in general, this tensor will have one positive eigenvalue and one negative one. We choose to represent such a tensor by two orthogonal lines, as shown in figure 5(a). The positive (negative) eigenvector represent the direction and amplitude of traction (compression) of deformed bubbles compared to the reference state. We also use this representation for the deformation rate which, like the statistical elastic strain, is an almost traceless tensor, since the flow remains weakly compressible. Here, the positive

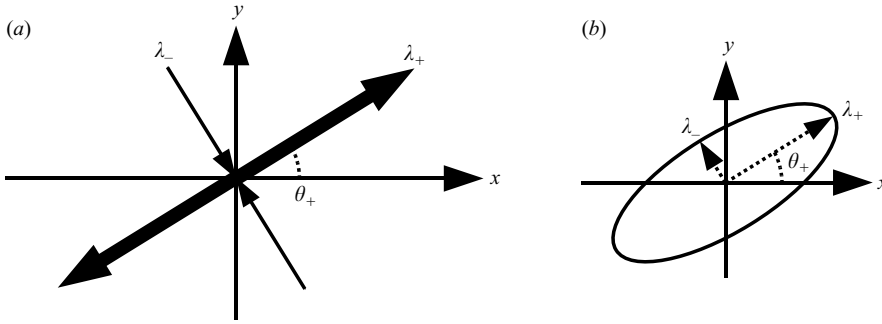


FIGURE 5. Representation of symmetric tensors (i.e. with orthogonal eigenvectors): (a) representation of a tensor with two eigenvalues of different sign ($\lambda_- < 0 < \lambda_+$). The thick (thin) line represents the direction and magnitude of the positive (negative) eigenvalue; (b) elliptic representation of a tensor with strictly positive eigenvalues ($0 < \lambda_- < \lambda_+$).

(negative) eigenvector represent the direction and amplitude of maximal elongation (compression) rate.

Finally, we represent the T1s by the two tensors $\mathbf{T}_+^{\text{adim}}$ and $\mathbf{T}_-^{\text{adim}}$ (§2.2.2), which are symmetric with strictly positive eigenvalues; they are therefore suitably represented by ellipses (figure 5b) of parameterized equations:

$$\begin{pmatrix} x_{\pm}(t) \\ y_{\pm}(t) \end{pmatrix} = \mathbf{T}_{\pm}^{\text{adim}} \cdot \begin{pmatrix} \cos t \\ \sin t \end{pmatrix} = \begin{pmatrix} (T_{\pm}^{\text{adim}})_{xx} \cos t + (T_{\pm}^{\text{adim}})_{xy} \sin t \\ (T_{\pm}^{\text{adim}})_{xy} \cos t + (T_{\pm}^{\text{adim}})_{yy} \sin t \end{pmatrix}.$$

In this case, the major axis is the preferred direction for T1s to occur. We justify this (new) way to quantify T1s in §3.2.5.

3. Results

In this section, we present the local measurements for a foam flowing around an obstacle. We first focus on a reference case: the flow of a monodisperse foam (bubble area: 16.0 mm², foam thickness: 3.5 mm, bulk viscosity: 1.06 mm² s⁻¹, flow rate: 176 ml min⁻¹) around a circular obstacle of diameter 30 mm. We compare averages and fluctuations of a local field to show that the foam behaves like a continuous medium (§3.1). We then present a full study of the reference case (§3.2), and separate the influence of each control parameter (§3.3).

3.1. Averages versus fluctuations

Can we consider the foam as a continuous medium in our case? This is not obvious *a priori*, since the steady flow arises from a balance between the load experienced by the bubbles passing around the obstacle and the discrete relaxations occurring during T1 events (Langer & Liu 1997): locally defined quantities such as elastic stress or statistical elastic strain fluctuate around an average value. We consider here the influence of such fluctuations and their correlations, since various studies in cylindrical Couette geometries have shown their great importance, especially when T1 ‘avalanches’ occur (Debrégeas *et al.* 2001; Kabla & Debrégeas 2003), leading to large stress drops (Lauridsen *et al.* 2002; Pratt & Dennin 2003).

To address this question, we analyse the temporal fluctuations of a local quantity for our reference case, in the same spirit as Janiaud & Graner (2005). We have chosen the statistical elastic strain tensor \mathbf{U} , but the analysis would be similar for other local quantities such as velocity or pressure. More precisely, we have chosen to

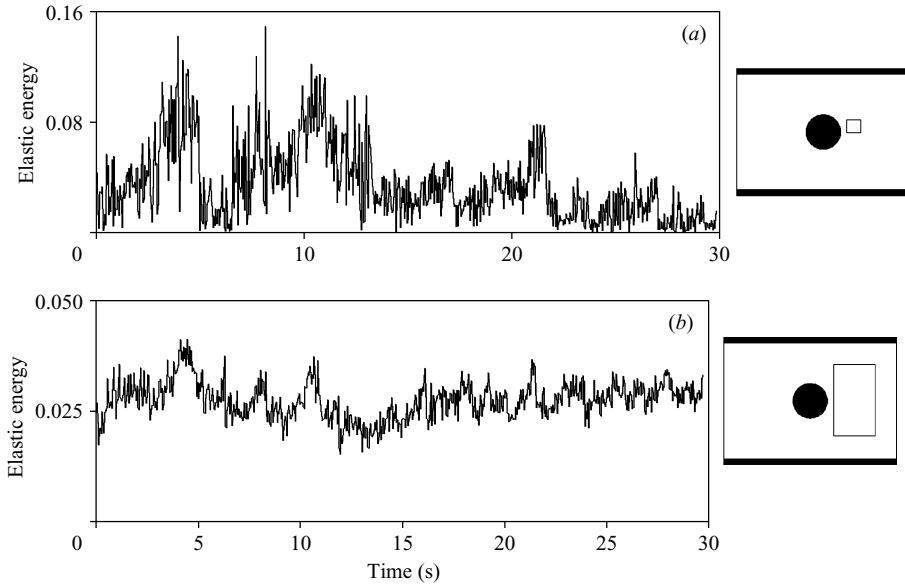


FIGURE 6. Temporal evolution of $[\lambda_+(\mathbf{U}) - \lambda_-(\mathbf{U})]^2$, which scales as the elastic energy. (a) Results for a box of size $1.2 \times 1.1 \text{ cm}^2$ (sketched at the right side). (b) Results for a box of size $3.6 \times 6.2 \text{ cm}^2$.

analyse one scalar quantity extracted from \mathbf{U} : the square of the difference between the two eigenvalues $[\lambda_+(\mathbf{U}) - \lambda_-(\mathbf{U})]^2$. Since \mathbf{U} is proportional to the elastic stress up to large deformation within 2% (see §2.3.3), this quantity scales as the elastic energy associated with shear strain; hence, it is expected to exhibit very large drops if T1 avalanches occur, since they release a lot of elastic energy. We have analysed the fluctuations in a box close to the trailing side of the obstacle (figure 6a, right), where fluctuations are expected to be strong; we will see later that this is also a region where T1s are frequent. The temporal variation of the elastic energy is reported in figure 6(a). Qualitatively, we do not observe a behaviour dominated by T1 avalanches: it would correspond to a succession of small increases (load) and fast decreases (relaxation) of the elastic energy. Quantitatively, we analyse the increments of the bubble deformation between two successive images, and show the histogram of the distribution of these increments in figure 7(a). This histogram is fitted well by a Gaussian curve, characteristic of a white noise, and we do not observe an asymmetric distribution with the many small increases and a smaller number of large decreases, which would correspond to T1 avalanches.

However, the box considered is small, where only seven bubbles in average are present at a given instant. One could thus argue that fluctuations are dominated by advection, not by possible T1 avalanches occurring at larger scale. We thus analyse the fluctuations at a larger scale, choosing a box 18 times bigger, in the wake of the obstacle (figure 6b, right). The relative fluctuations are much smaller (figure 6b), and the increments are here again fitted well by a Gaussian curve (figure 7b).

We have performed this quantitative analysis of the fluctuations only in our reference experiment, but we observed in the other experiments analysed here that the fluctuations do not present large-scale correlations; they are similar to a random, white noise and play a negligible role at large scales. We will thus only focus on

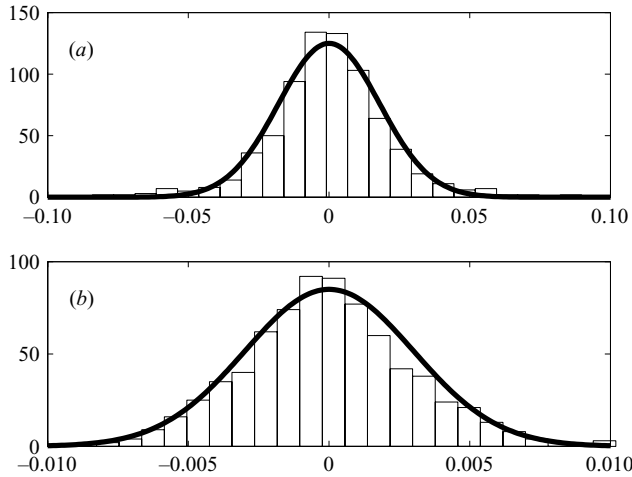


FIGURE 7. Histogram of the increments of $[\lambda_+(\mathbf{U}) - \lambda_-(\mathbf{U})]^2$. (a) Results for a box of size $1.2 \times 1.1 \text{ cm}^2$ (average: 3.7×10^{-5} , standard deviation: 1.8×10^{-2}). (b) Results for a box of size $3.6 \times 6.2 \text{ cm}^2$ (average: -8.4×10^{-6} , standard deviation: 3.0×10^{-3}). The curves superimposed are Gaussian curves with the same mean and standard deviation as the histograms.

coarse-grained average quantities, and treat the foam as a continuous medium. The generality of such an approach is discussed in §4.1.

3.2. Study of a reference case

For each field studied, we proceed as follows: we first present a map of the whole field, and we then study the variation of the field components along various lines: two directed streamwise, one being on the axis of the obstacle and the other beside it, 2.5 cm from the axis of symmetry of the flow; and three directed spanwise, one passing through the centre of the obstacle, one upstream and a symmetric downstream one, both lines being 2.4 cm from the middle axis (figure 8).

3.2.1. Velocity

The whole velocity field is presented in figure 9. Qualitatively, the flow far from the obstacle is a plug flow, as already observed for foam flows in narrow channels (Cantat, Kern & Delannay 2004). The obstacle imposes two symmetric stagnation points, one upstream and one downstream, and the flow is constricted, and thus accelerated, at the sides of the obstacle.

To study the velocity quantitatively, we divide it by the averaged velocity v_0 obtained from the upstream and downstream extremities of the observation region, where the flow is less perturbed: v_0 is therefore the velocity of the plug flow. We report the two components of $(\mathbf{v} - v_0)/v_0$, which is the dimensionless velocity deviation from the plug flow, in figure 10. This figure shows a striking feature: the velocity is fore-aft asymmetric. More precisely, on the axis $y=0$, the component v_x has an overshoot downstream, in the wake of the obstacle, whereas it varies monotonically upstream. The asymmetry is also obvious in the comparison of v_x between the axes $x = -2.4$ and 2.4 cm : the perturbation from the plug flow is higher upstream than downstream for v_x , and vice versa for v_y . As expected, the v_y component vanishes on the $y=0$ axis.

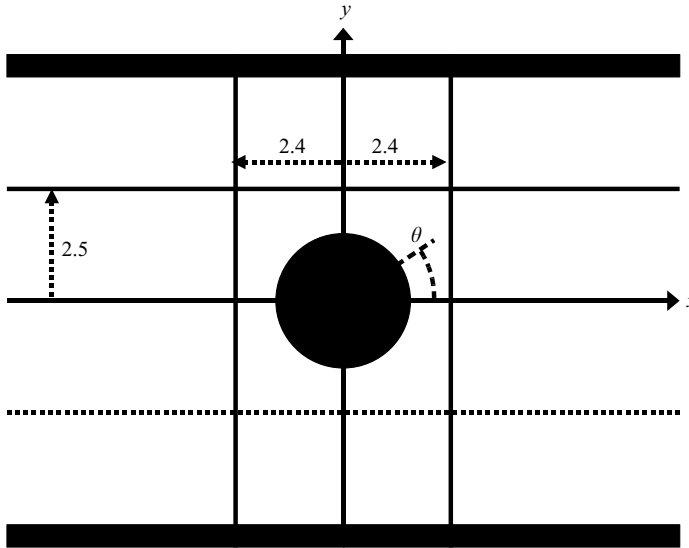


FIGURE 8. Sketch of the lines along which the fields are evaluated. The streamwise direction is x , the spanwise is y . We choose five lines: the axis of symmetry of the flow, $y=0$; an axis at the side of the obstacle, $|y|=2.5$ cm (the dashed axis means that there are two such symmetric axes; the evaluated quantities will be averaged on these both axes); and three axes perpendicular to the flow direction: $x=-2.4, 0$ and 2.4 cm.

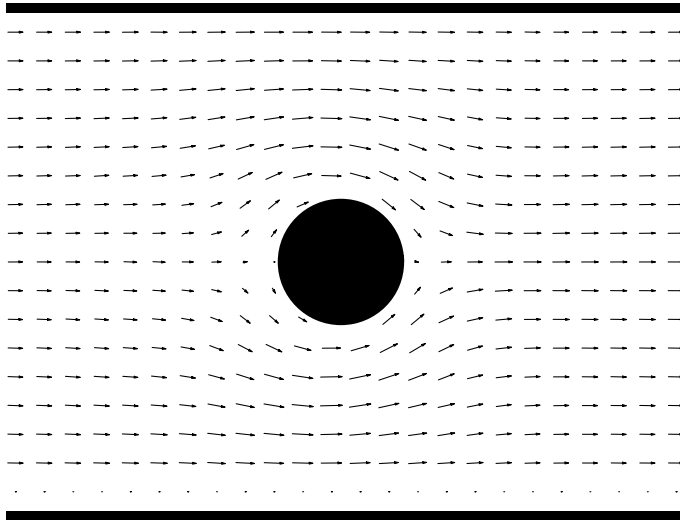


FIGURE 9. Velocity field around a circular obstacle.

3.2.2. Pressure

The whole pressure field is presented in figure 11. The pressure is maximal at the leading side of the obstacle, and minimal at its trailing side. We can also note that the increase in pressure upstream is very progressive, extending farther than the limits of the observation field. Figure 12 displays the evolution of the pressure along the five axes of figure 8. We also observe a fore-aft asymmetry; unlike the velocity, this asymmetry is more obvious on the side of the obstacle than on the axis $y=0$: the

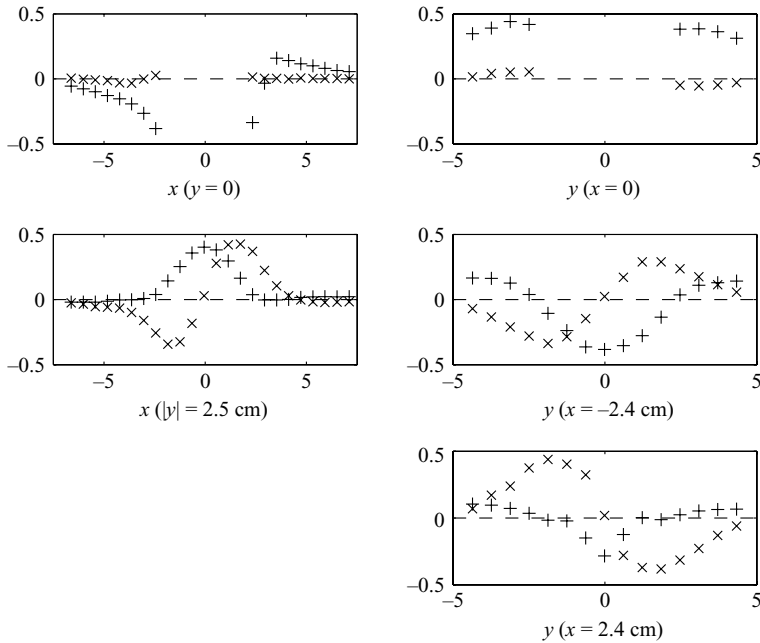


FIGURE 10. Velocity components around a circular obstacle: $(v_x - v_0)/v_0$ (+), and v_y/v_0 (x), along the axes shown in figure 8. The length unit is centimetres.

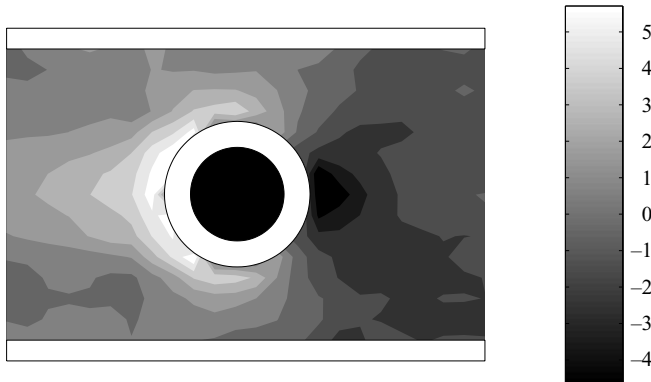


FIGURE 11. Pressure field around a circular obstacle, expressed in Pa. The higher the pressure, the darker the grey level. In the white regions, the bubble area, hence the pressure, cannot be reliably evaluated.

pressure perturbation changes sign at $y = 2$ cm. Note also that along the axis $x = 0$, the decrease of the perturbation in pressure with the distance to the obstacle is faster than the perturbation in velocity.

3.2.3. Statistical elastic strain

We now study the statistical elastic strain field, defined by (2.4), to quantify the bubble deformation, as explained in §2.3.3. We display this field in figure 13 using the representation explained in figure 5(b). We note that the deformation is not negligible for the bubbles entering the observation field: they are slightly stretched in the spanwise direction. The bubbles are stretched in the x -direction at the sides and

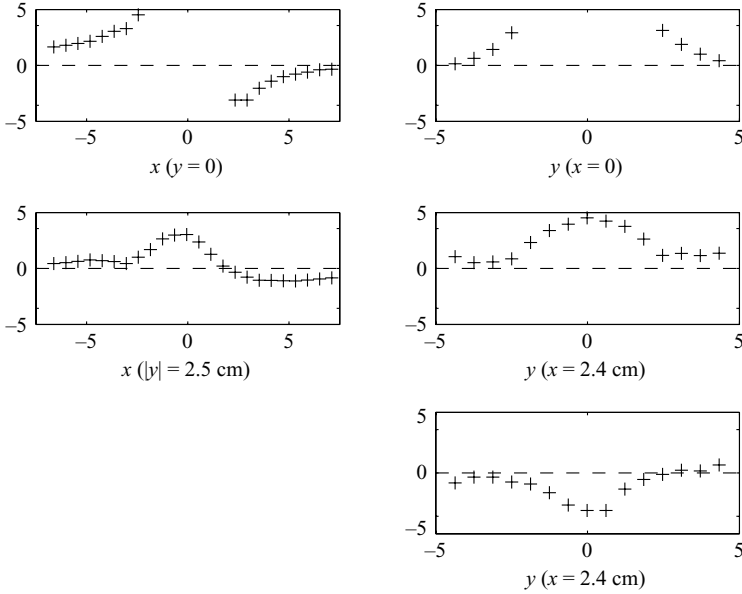


FIGURE 12. Pressure evolution (in Pa) around a circular obstacle. The pressure is evaluated from (2.2); more precisely, we report here the difference between the local pressure and an average one corresponding to the average bubble area A_0 .

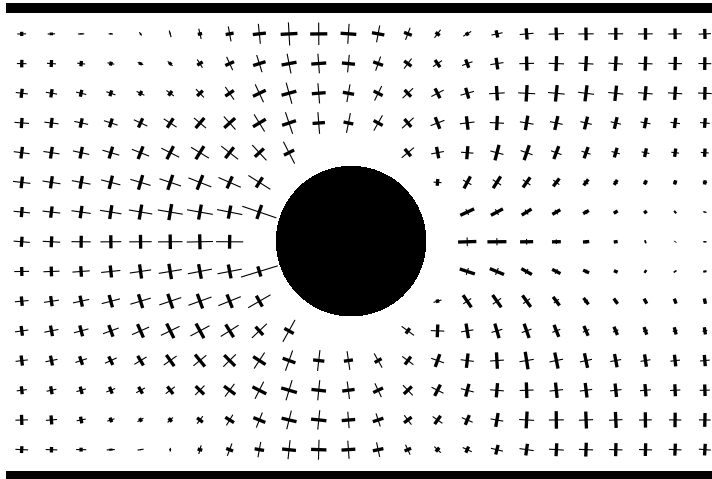


FIGURE 13. Statistical elastic strain field around a circular obstacle. The thick (thin) line is a direction of maximal elongation (compression), see figure 5(a).

in the wake of the obstacle, and in the y -direction at the leading side of the obstacle and at the sides of the wake.

The statistical elastic strain field \mathbf{U} is a symmetric tensor, hence it has three independent components U_{xx} , U_{xy} and U_{yy} . Instead of these three components, we have chosen to represent the combinations $U_{xx} + U_{yy}$, $U_{xx} - U_{yy}$ and U_{xy} . The trace $U_{xx} + U_{yy}$ gives access to the dilatation, whereas the difference $U_{xx} - U_{yy}$ compares the bubble deformation in the directions parallel and perpendicular to the flow, and the U_{xy} component indicates the deviation of the deformation from the x - and

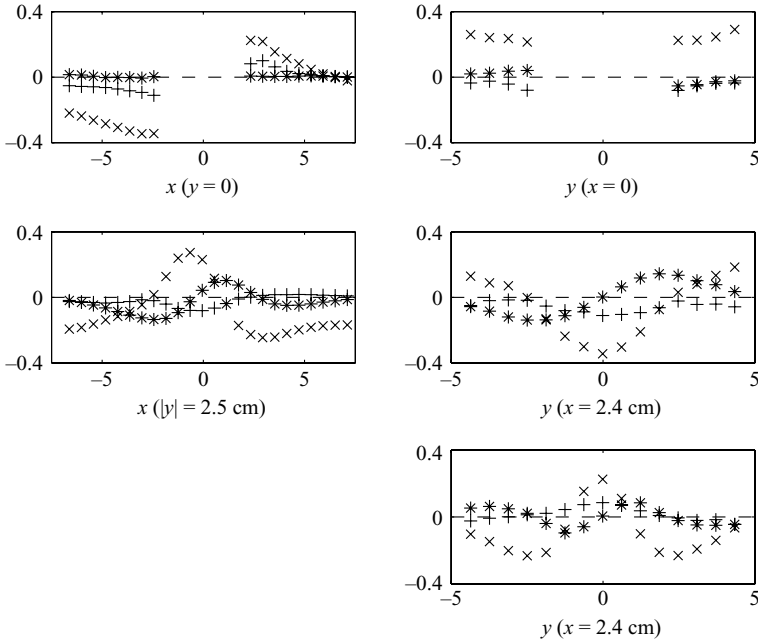


FIGURE 14. Combinations $U_{xx} + U_{yy}$ (+), $U_{xx} - U_{yy}$ (x) and U_{xy} (*) of the statistical elastic strain field around a circular obstacle.

y-directions. These combinations are plotted in figure 14 along the five axes of figure 8. First, the trace has a weak amplitude (its absolute value remains lower than 0.1), and its evolution is strongly anti-correlated to the pressure (figure 12). The explanation of such a trend is easy: when the pressure increases, the bubble area decreases as explained in § 2.3.1. Hence, the length of the vectors \mathbf{r} linking centres of neighbouring bubbles decreases, and so does $U_{xx} + U_{yy} \approx \ln r/r_0$ from equation (2.4).

Second, we consider the parameter $U_{xx} - U_{yy}$. It tends towards a negative value far from the obstacle, which confirms the spanwise stretch observed on figure 13. This trend is observed both upstream and downstream, hence it is probably due to the longitudinal pressure gradient due to the pressure drop along the channel. More interestingly, the presence of the obstacle strongly modifies the deformation of the bubbles: considering the downstream axis ($x = 2.4$ cm), the bubbles are stretched streamwise in the wake, and spanwise at the sides of the wake, the transition occurring at $|y| = 1.5$ cm. On the other hand, on the upstream axis ($x = -2.4$ cm) the bubbles are stretched spanwise close to the symmetry axis of the flow, and streamwise at the sides, the transition occurring at $|y| = 2$ cm.

Third, the U_{xy} component at the sides of the obstacle ($|y| = 2.5$ cm) changes sign at two different points ($x = 0$ and 2 cm), showing that the orientation of the maximal deformation rotates about 180° during the passage around the obstacle. Note also that this component is not strictly reversed between upstream and downstream (compare of the axes $x = -2.4$ and $y = 2.4$ cm).

3.2.4. Velocity gradients

We now turn to the velocity gradients. We first show the map of the deformation rate in figure 15. It confirms that the two-dimensional effective compressibility of the flow (see § 2.3.1) remains weak, because the absolute value of maximal elongation and

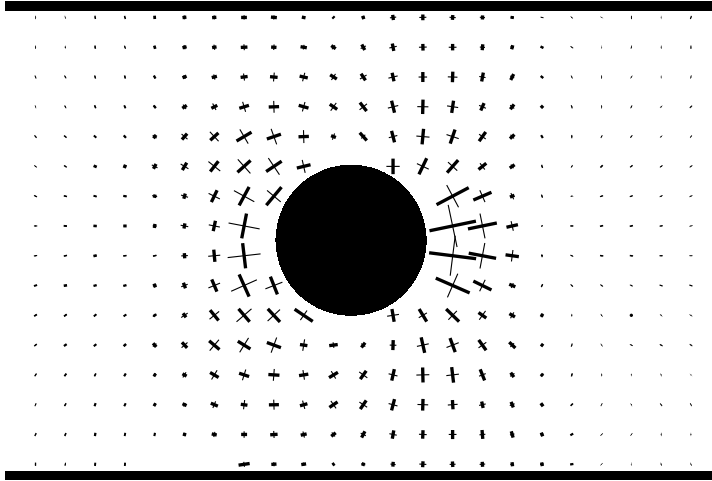


FIGURE 15. Deformation rate field around a circular obstacle. The thick (thin) line represents the maximal elongation (compression) rate, see figure 5(a).

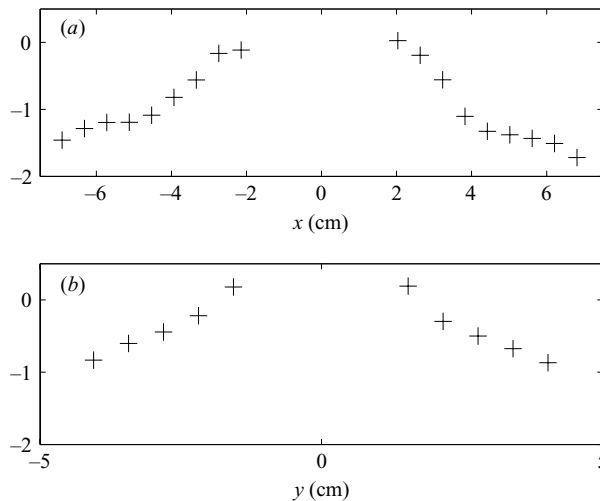


FIGURE 16. Logarithm of the dissipation function, defined as (2.3) and expressed in s^{-1} , as a function of x on the $y=0$ axis (a), and as a function of y on the $x=0$ axis (b).

the maximal compression are very close at any point. Furthermore, the amplitude of the deformation rate decreases quickly with the distance from the obstacle, and seems to become negligible upstream and downstream at a distance comparable with the obstacle diameter. To investigate whether this amplitude really vanishes at a finite distance from the obstacle, as expected for a Bingham plastic in the same flow conditions (Mitsoulis 2004), we consider the (scalar) dissipation function defined in (2.3), and plot its logarithm along the two symmetry axes $x=0$ and $y=0$ (figure 16). This plot reveals that the dissipation function decreases with the distance from the obstacle, but does not vanish. It is possible that it vanishes farther from the obstacle, but we have not investigated this possibility. Furthermore, the decrease is more complex than a power-law or exponential decrease, and is faster downstream than upstream.

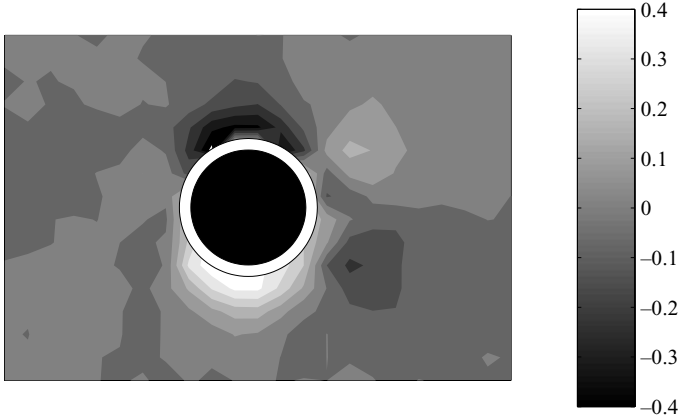


FIGURE 17. Vorticity field around a circular obstacle, expressed in s^{-1} . The light (dark) grey levels represent positive (negative) vorticity.

The map of the vorticity presented in figure 17. exhibits significant variations, antisymmetric with respect to the $y=0$ axis: in the $y > 0$ half-channel, it is negative at the side of the obstacle, and positive downstream. The fore–aft asymmetry is once again obvious. Unlike potential flows, the vorticity is a significant component of the velocity field: its maximum, $0.4 s^{-1}$, is of the same order of magnitude as the deformation rate ($1 s^{-1}$ from figure 16).

3.2.5. T1 quantification

We first investigate the validity of our measurements of T1s. As explained in § 2.2.2, the calculation of appearing and disappearing edges is decoupled; therefore, we have to check whether the number of these two kinds of events is the same, as it should be if we record the T1s correctly. Furthermore, we emphasize that our method may be sensitive to artifacts. We have calculated the following quantity:

$$\frac{\sum_{\text{every box } i} |f_+ - f_-|_i}{\sum_{\text{every box } i} (f_+ + f_-)_i} = 7.0 \%, \quad (3.1)$$

which quantifies the relative uncertainty of our method, which is acceptable despite the various sources of errors.

We now represent the map of T1s in figure 18, which illustrates the advantages of the tensorial representation: not only does it contain the number of T1s (proportional to the size of the ellipses, as discussed in § 2.2.2), but also their direction. The major axes of the two kinds of ellipses are mainly orthogonal, which illustrates the fact that plastic events release high stresses from one direction to the perpendicular direction (Picard *et al.* 2004). Quantitatively, denoting as \mathbf{x}_+ (\mathbf{x}_-) the unit vector of the major axis of the ellipse representing $\mathcal{T}_+^{\text{adim}}$ ($\mathcal{T}_-^{\text{adim}}$), we calculate for each box the scalar product $\mathbf{x}_+ \cdot \mathbf{x}_-$, and show the histogram of this quantity in figure 19. It is strongly peaked around 0, confirming that \mathbf{x}_+ and \mathbf{x}_- are orthogonal. We also calculate the average and standard deviation of the scalar product $\mathbf{x}_+ \cdot \mathbf{x}_-$, weighted by the number of T1s for each box: $\langle \mathbf{x}_+ \cdot \mathbf{x}_- \rangle = 7.6 \times 10^{-5}$ and $\delta(\mathbf{x}_+ \cdot \mathbf{x}_-) = 1.4 \times 10^{-2} \ll 1$, which proves the orthogonality of appearing and disappearing edges.

Figure 18 shows that T1s are concentrated close to the obstacle, but again with a significant asymmetry: upstream, the T1s are more distributed and spread widely over the sides of the obstacle, whereas downstream they are more localized in the

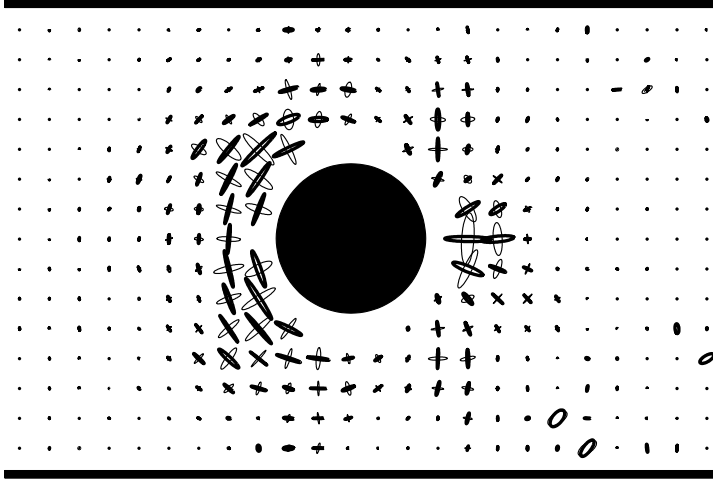


FIGURE 18. Elliptical representation of T1s: the thin (thick) ellipses represent the tensor $\mathbf{T}_+^{\text{dim}}$ ($\mathbf{T}_-^{\text{dim}}$), defined in §2.2.2. The preferred direction of the T1s is obvious in the tensorial representation. Note the few remaining artifacts (bottom right).

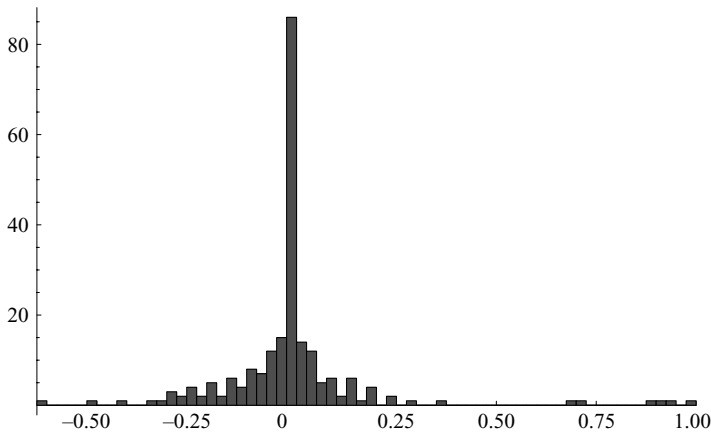


FIGURE 19. Distribution histogram of $\mathbf{x}_+ \cdot \mathbf{x}_-$ (see text for definition).

wake. Note also that the direction of T1s is correlated with those to the ones of the statistical elastic strain (figure 13) and of the deformation rate (figure 15); such a correlation is probably important in understanding better the rheology of foams.

To focus on the spatial distribution of the frequency of T1s, we now plot $\|\mathbf{T}_+^{\text{dim}} - \mathbf{T}_-^{\text{dim}}\|/\sqrt{2}$. When $\mathbf{x}_+ \cdot \mathbf{x}_- = 0$, which is a good approximation, this quantity equals $(f_+ + f_-)/2$; we thus identify it with the frequency of T1s per link (which is also the inverse of the average lifetime of a given link). This quantity has the advantage of reducing strongly the remaining artifacts; it is mapped on figure 20. This map shows that the T1 frequency presents three maxima: one centred in the wake, and two symmetrically off-centred downstream, at an angular position $|\theta| \simeq 3\pi/4$ (see figure 8 for the definition of θ). The complex angular dependence of the T1 frequency is illustrated on figure 21. It shows that the off-centred downstream maximum arises for an angle $\theta = 145^\circ$, and that the frequency of T1s is almost equal for this maximum

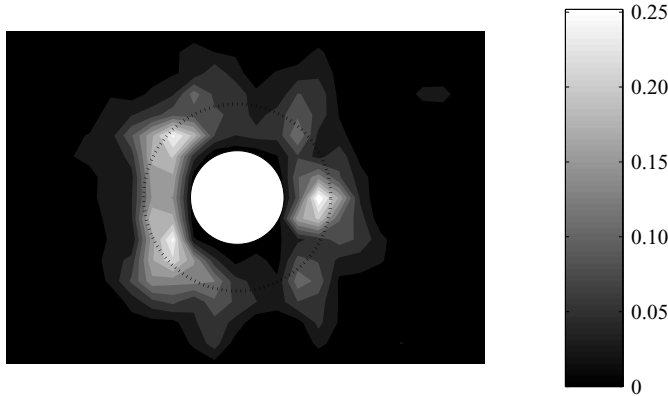


FIGURE 20. Spatial distribution of the frequency of T1s, expressed in s^{-1} . The lighter the grey lever, the higher the frequency of T1s. Note the attenuation of the artifacts in comparison with figure 18, as well as the marked fore–aft asymmetry. The dotted circle indicates the position chosen for the evaluation of figure 21.

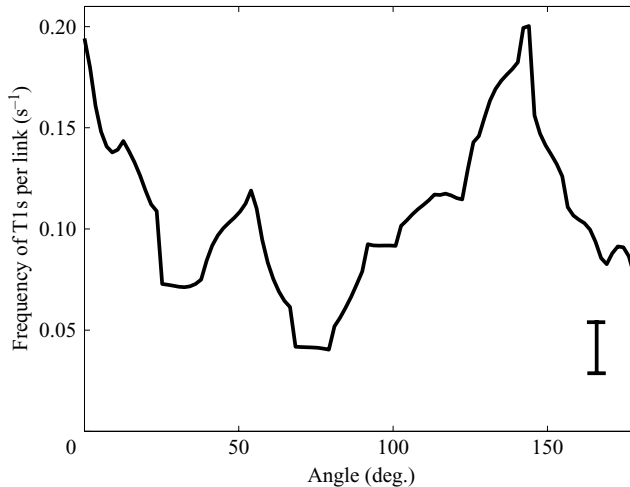


FIGURE 21. Angular dependence (in degrees) of the frequency of T1s per unit link, evaluated 1.5cm from the boundary of the obstacle. The flow being symmetric with respect to the axis $y=0$, the data have been averaged for the angles between -180° and 0 . The estimated error bar is drawn at the bottom right of the plot: according to the evaluation of the experimental uncertainty (3.1), we estimate it as at most $\pm 7\%$ of the maximum T1 frequency, which ensures that the secondary maximum at 40° and the secondary minimum at 55° are significant extrema.

and for the one located in the wake, with a value of $0.2 s^{-1}$. Figure 21 shows also a secondary maximum for $\theta = 55^\circ$.

3.3. Influence of various control parameters

In this section, we systematically study the fields describing the flow of foams around obstacles in the same spirit as in Dollet *et al.* (2005c): starting from the reference experiment extensively studied in the previous section, we vary only one control parameter at a time, successively the flow rate (§ 3.3.1), the bubble area (§ 3.3.2), the foam thickness (§ 3.3.3) and the bulk viscosity (§ 3.3.4). To simplify the discussion, we only study the evolution of three scalar quantities: the velocity component v_x , the

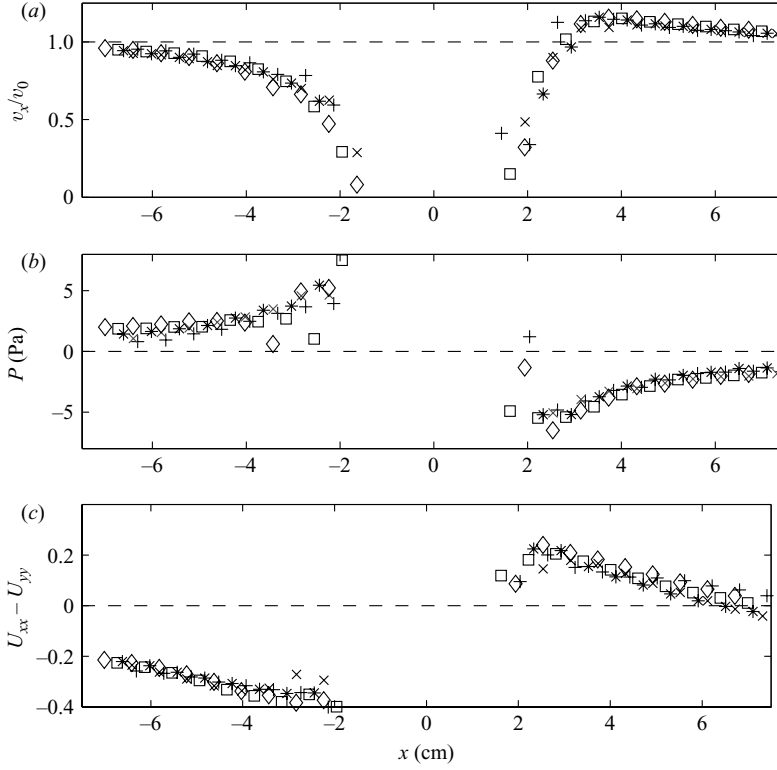


FIGURE 22. Plots of (a) the dimensionless velocity v_x/v_0 , (b) the pressure, and (c) the component $U_{xx} - U_{yy}$, as a function of x along the axis $y=0$, for flow rates of 24 (+), 54 (\times), 176 (*), 293 (\square) and 515 ml min^{-1} (\diamond).

pressure P and $U_{xx} - U_{yy}$, along the axis of symmetry $y=0$. We end this section by discussing the influence of the size and roughness of the obstacle (§ 3.3.5).

3.3.1. Flow rate

For a given bubble area (16.0 mm^2), foam thickness (3.5 mm) and bulk viscosity ($1.06 \text{ mm}^2 \text{ s}^{-1}$), we study five different flow rates: 24, 54, 176, 293 and 515 ml min^{-1} (corresponding velocities v_0 : 0.11, 0.26, 0.84, 1.40 and 2.45 cm s^{-1}). To compare the velocities more easily, we consider the dimensionless velocity v_x/v_0 which is plotted, as well as the pressure and the component $U_{xx} - U_{yy}$, along the axis $y=0$, in figure 22. Remarkably, all data points collapse on the same master curve for the velocity, the pressure and the bubble deformation, which proves that the qualitative features found in § 3.2 do not change in the range of flow rate studied.

3.3.2. Bubble area

To study the influence of bubble area, the flow rate cannot be strictly imposed, since it is slaved to target values of the other control parameters. However, as shown in § 3.3.1, it has no significant influence on the results. We study for each bubble area: 12.1, 16.0, 20.0, 25.7, 31.7 and 39.3 mm^2 , a flow rate as close as possible to the reference case, respectively 160, 176, 166, 133, 150 and 169 ml min^{-1} . The results are reported in figure 23. They show that neither the velocity field nor the bubble deformation depends qualitatively on the bubble area. Only the pressure behaviour in the wake changes: for big enough bubbles, the pressure release at the trailing side observed in

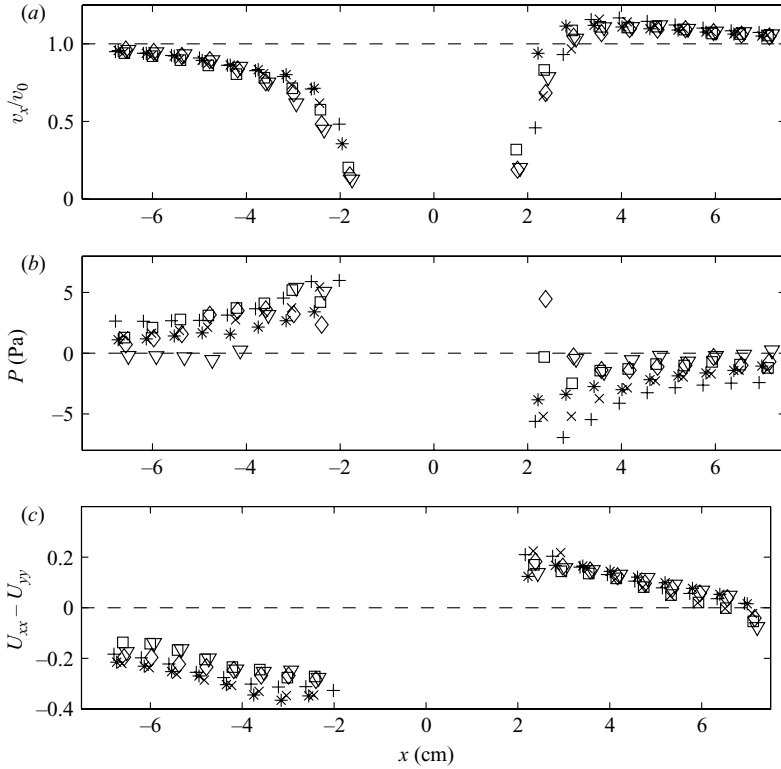


FIGURE 23. Plots of (a) the dimensionless velocity v_x/v_0 , (b) the pressure, and (c) the component $U_{xx} - U_{yy}$, as a function of x along the axis $y=0$, for bubble areas of 12.1 (+), 16.0 (\times), 20.0 (*), 25.7 (\square), 31.7 (\diamond) and 39.3 mm² (∇).

figure 12 occurs farther downstream, and can be preceded by a compression zone close to the obstacle.

3.3.3. Foam thickness

Various theoretical (Princen 1983; Khan & Armstrong 1986) and experimental (Princen 1985; Mason, Bibette & Weitz 1995, 1996; Saint-Jalmes & Durian 1999) studies have shown that the fluid fraction plays a crucial role in the foam rheology, but its influence on the behaviour of the foam at the local scale has been less studied (Durian 1997). In our case, the foam thickness is a way to change the fluid fraction of the foam: an increasing foam thickness corresponds to a drier foam. We study six different foam thicknesses: 2.0, 2.5, 3.0, 3.5, 4.0 and 4.5 mm, at fixed bubble area 16.0 mm². The corresponding fluid fractions are estimated as (Raufaste *et al.* 2007): 6.2%, 5.9%, 4.3%, 4.3%, 4.1% and 3.6%. Since the cross-section of the foam varies proportionally to its thickness, we choose a mean velocity v_0 (see §3.2.1) closest as possible to the reference case, respectively 0.67, 0.88, 0.89, 0.84, 0.74 and 0.56 cm s⁻¹ for the six thicknesses. Velocity, pressure and bubble deformation are plotted in figure 24. We observe the following variations for the lowest foam thicknesses (or highest fluid fractions): the asymmetry in the velocity is weaker, a compression zone appears in the wake close to the obstacle (as for the biggest bubbles studied in §3.3.2), and the amplitude of the bubble deformation decreases. Note that there are no significant variations for

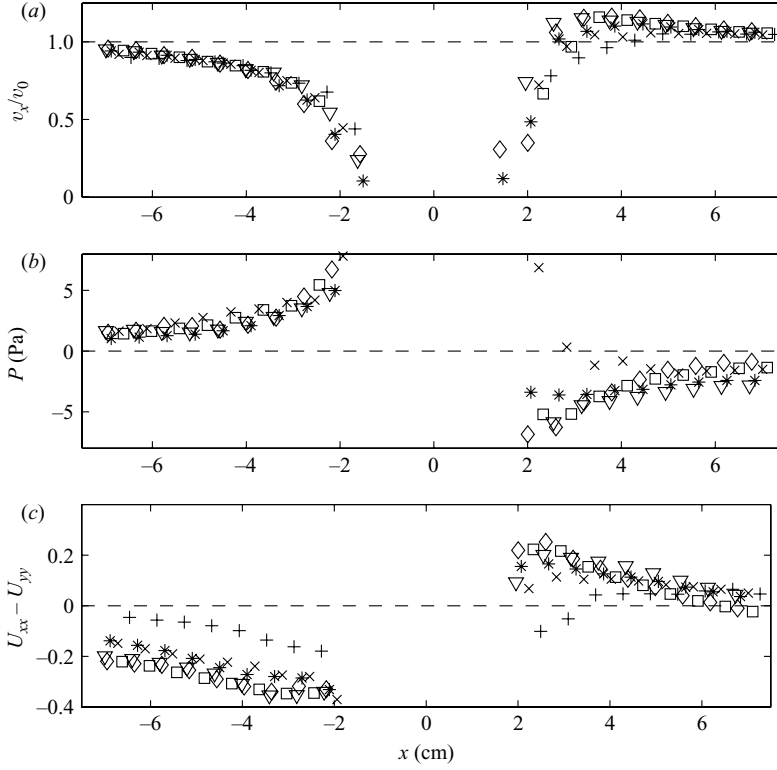


FIGURE 24. Plots of (a) the dimensionless velocity v_x/v_0 , (b) the pressure, and (c) the component $U_{xx} - U_{yy}$, as a function of x along the axis $y=0$, for foam thicknesses of 2.0 (+), 2.5 (\times), 3.0 (*), 3.5 (\square), 4.0 (\diamond) and 4.5 cm (∇). Since the bubbles are separated, the pressure cannot be calculated for the foam thickness of 2.0 mm.

the three highest thicknesses, probably because the corresponding fluid fractions are very similar.

3.3.4. Bulk viscosity

We now investigate the influence of bulk viscosity. Of the various cases studied in Dollet *et al.* (2005c), we only consider the two extremes ones: a soap solution without added glycerol (viscosity: $1.06 \text{ mm}^2 \text{ s}^{-1}$), and one with 50 % added glycerol by mass (viscosity: $9.3 \text{ mm}^2 \text{ s}^{-1}$). The bubble area is 20.0 mm^2 . The flow rates are 166 and 154 ml min^{-1} for the low and high viscosity cases. The results are presented on figure 25. They show that the bulk viscosity has no significant effect, except in the wake close to the obstacle.

To summarize this study of the influence of the following control parameters: flow rate, bubble area, foam thickness and bulk viscosity, we have shown that the main trends shown in the reference case (§ 3.2) are robust, especially the fore–aft asymmetry.

3.3.5. Obstacle size and boundary

The last control parameter that we have studied is the obstacle itself. We have shown in previous studies that tuning the obstacle geometry allows a variety of behaviours: streamlining for a symmetric airfoil profile (Dollet *et al.* 2005c) and anti-inertial lift for a cambered one (Dollet *et al.* 2005a), and a combination of drag, lift and torque for an elliptical obstacle (Dollet *et al.* 2006). Here, we focus on simpler, circular

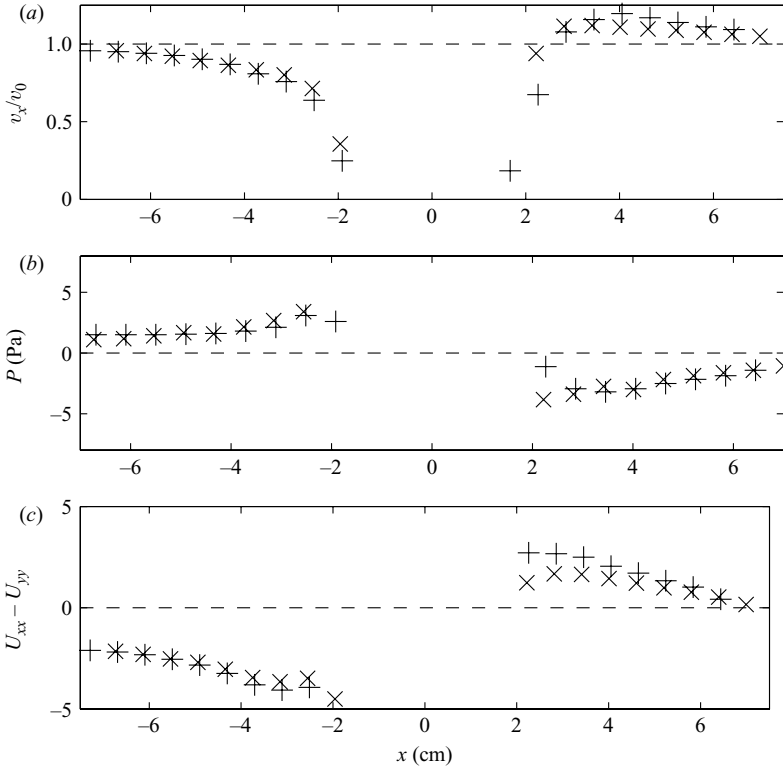


FIGURE 25. Plots of (a) the dimensionless velocity v_x/v_0 , (b) the pressure, and (c) the component $U_{xx} - U_{yy}$, as a function of x along the axis $y=0$, for bulk viscosities of 1.06 (\times), and $9.3 \text{ mm}^2 \text{ s}^{-1}$ ($+$).

shapes, and compare the reference obstacle, a circle of diameter 30 mm, to a bigger circle, of diameter 48 mm, and a cogwheel of diameter 43.5 mm with cogs of length 4 mm. The other control parameters are the same as in the reference experiments: foam thickness of 3.5 mm, bulk viscosity of $1.06 \text{ mm}^2 \text{ s}^{-1}$ and bubble area of 16.0 mm^2 . This area is suitable for bubbles to be trapped in the cogs of the cogwheel, defining an effective circular obstacle constituted by the cogwheel and the trapped bubbles, of diameter 47.5 mm, comparable to the big circle. In this section, we thus study the influence of the size and the boundary of the obstacle. As these obstacles share the circular symmetry, we choose to study them in polar coordinates, plotting the components v_r and $-v_\theta$ of the velocity, the pressure, and the deviatoric component of the statistical elastic strain tensor $U_{rr} - U_{\theta\theta}$, as functions of θ along a circle located 1.5 cm from the obstacle boundary (figure 26).

The data for the big circle and the cogwheel are very similar, showing that the boundary conditions have little influence on the behaviour of the foam. The comparison between the two circles shows that whereas the radial component of the velocity is almost equal, the amplitude of the azimuthal component is bigger for the bigger circle. This is a consequence of the constriction between the obstacles and the channel walls: more precisely, at the angle $\theta = 90^\circ$, we have $-v_\theta/v_0 = v_y/v_0 = 1.83$ for the circle of diameter 48 mm, and $-v_\theta/v_0 = 1.41$ for the circle of diameter 30 mm, which is comparable to the aspect ratio $h/(h-D)$, with $h = 10$ cm the channel width and D the obstacle diameter, which equals 1.92 and 1.43 for these two circles. Also, whereas

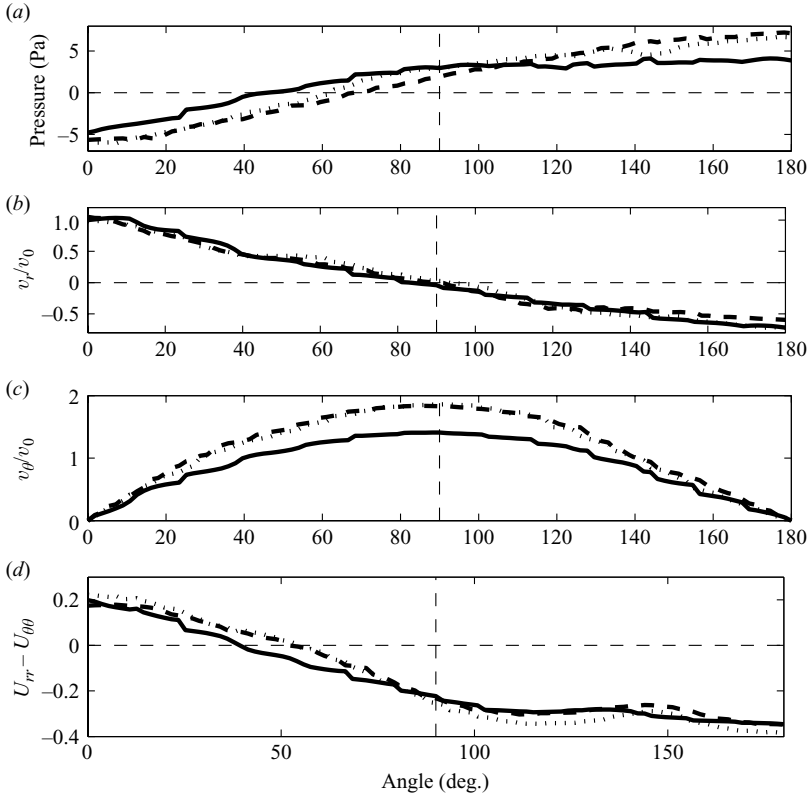


FIGURE 26. Plots of (a) the pressure, (a, c) the components v_r/v_0 and $-v_\theta/v_0$ of the dimensionless velocity, and (d) the component $U_{rr} - U_{\theta\theta}$ of the statistical elastic strain, for circles of diameter 30 mm (solid line) and 48 mm (long-dashed line), and the cogwheel (dotted line) as a function of the angle θ , between 0 and 180°. The flow being symmetric with respect to the axis $y=0$, the data have been averaged for the angles between -180° and 0.

the amplitude of variation of the pressure is weaker for the small circle, the statistical elastic strain component $U_{rr} - U_{\theta\theta}$ does not change much for the three obstacles. It is negative and almost constant for angles between 100° and 180° (figure 26), which corresponds to an extended region where the yield strain is reached; the component $U_{rr} - U_{\theta\theta}$ has a markedly different behaviour for angles between 0 and 100°, where it follows a monotonic, almost linear evolution, which is the signature of an elastic-like transition to another yielded region, located in the wake of the obstacle. This is confirmed by the polar dependence of the frequency of T1s (figure 21), which shows a high frequency in the yielded regions for angles close to 0 and between 100° and 180°, and lower frequency in between. A simple sketch of this behaviour, with a yielded region on the whole leading side of the obstacle and an elastic transition at the trailing side to another yielded region in the wake, helps in understanding the fluid fraction dependence of the drag on circles (Raufaste *et al.* 2007) as well as the angular dependence of the drag, lift and torque experienced by an ellipse (Dollet *et al.* 2006).

4. Discussion

4.1. Liquid foam: localization or continuity?

Our analysis of §3.1, showing that the fluctuations are like a white noise, suggests that the foam behaves as a continuous medium. We did not measure large-scale

correlations of plastic rearrangements. This is to be compared to flows involving pure shear, such as experiments in Couette geometry (Debrégeas *et al.* 2001; Lauridsen *et al.* 2002; Pratt & Dennin 2003), in which a disordered and wet foam in a Hele-Shaw cell exhibits a strong discontinuity in the form of a localized shear band (Debrégeas *et al.* 2001), resulting from large-scale avalanches of T1 (Kabla & Debrégeas 2003), whereas a disordered and wet bubble raft shows no such bands (Lauridsen, Chanan & Dennin 2004). This suggests that velocity discontinuities in two-dimensional flowing foams are due to the friction between the bubbles and the confining boundaries. This is supported by a recent study which has shown that at given flow rate in a simple shear geometry, liquid pool foams exhibit localization, unlike bubble rafts (Wang *et al.* 2006), and by recent models for simple shear (Janiaud *et al.* 2006) and cylindrical Couette geometries (Clancy *et al.* 2006)

However, our liquid pool foam does not exhibit localization, and the velocity varies smoothly everywhere (figure 9). We did not observe avalanches of T1s, except for very wet and ordered foams, where dislocations between rows of bubbles can occur over distances of several centimetres. In the experiments presented here, this only occurs for the smallest foam thickness. Furthermore, both the duration of a T1 (i.e. the lifetime of the transient, unstable four-fold vertex) and the relaxation time τ_{T1} after a T1 (i.e. the time required for the foam to recover local equilibrium) are very short in our set-up. With our camera at 25 frames per second, we capture only a few four-fold vertices, hence the duration of a T1 is lower than 0.04 s on average; moreover, the relaxation after a T1 is too fast to be precisely estimated, and we can take $\tau_{T1} < 0.1$ s. This time is much shorter than the shortest time associated with velocity gradients, which equals $\tau_{v_v} = 1$ s (figure 16). Hence, the macroscopic continuity of the flow does not come from a microscopic continuity, which would occur if $\tau_{T1} < \tau_{v_v}$, where the foam ‘melts’ and the discontinuous character of T1s is suppressed (Gopal & Durian 1999). Two possible explanations for the qualitative difference between the flow in simple shear geometry (localization) and around an obstacle (continuity) are the more complex flow geometry induced by the presence of the obstacle, and the wall slip of the bubbles over the obstacle, whereas they are trapped at the boundaries in shear experiments. The latter point is supported by the fact that the velocity field around a smooth circle and a cogwheel are similar (figure 26). We indeed observe that the bubbles close to the cogwheel slip over the bubbles trapped in the cogs, which is reminiscent of shear banding.

4.2. Discussion of the reference experiment

4.2.1. Velocity

A salient and robust feature of the flow of foam around an obstacle is the fore–aft asymmetry of the velocity field. This asymmetry, and the velocity overshoot in the wake of the obstacle (figure 10), called a negative wake in the context of the sedimentation of particles, is well documented for viscoelastic and shear-thinning fluids, both in experiments (Hassager 1979; Arigo & McKinley 1998) and in simulations (Dou & Phan-Thien 2003; Kim *et al.* 2005). On the other hand, such an asymmetry is not captured by the classical models of yield-stress fluids usually invoked to simply model liquid foams, as shown by simulations of flows of Bingham plastics (Roquet & Saramito 2003; Mitsoulis 2004) or Herschel–Bulkley fluids (Beaulne & Mitsoulis 1997).

In the literature, little data about the velocity field of yield-stress fluids around an obstacle or a sedimenting particle exists, and only very recently have Gueslin *et al.* (2006) have reported a fore–aft asymmetry for a sphere sedimenting in a yield-stress

fluid (a Laponite suspension) and shown the presence of a negative wake provided the particle is heavy enough.

The exact explanation for the fore–aft asymmetry and the negative wake is not fully understood, but the proposed scenarios always involve extensional stresses, balanced either by shear stresses (Harlen 2002) or by normal stress differences (Bush 1994). To discard other possible reasons for the fore–aft asymmetry, specific to our set-up, note that the velocity boundary condition at the obstacle is different in our case (slip) and in the study of Gueslin *et al.* (2006) (no slip), hence it is probably not relevant for the asymmetry. The compressibility of the flow is probably not involved either, since it has been checked in other experiments and simulations that incompressible flows of foam around an obstacle present a negative wake (C. Raufaste and S. J. Cox, private communication). It would be interesting to check whether fore–aft asymmetry is also observed in other studies of foam flows, either in three-dimensional (de Bruyn 2004; Cantat & Pitois 2005) or in two-dimensional flows around a large bubble (Cantat *et al.* 2004; Cantat, Poloni & Delannay 2006), but these studies do not report detailed features of the velocity field.

4.2.2. Pressure

We showed that the pressure is maximal at the upstream side of the obstacle, and minimal at the downstream side (§ 3.2.2), and that it does not depend significantly on the flow rate (§ 3.3.1). This suggests that the pressure is mainly of elastic origin, which is also corroborated by the anti-inertial lift observed for an airfoil (Dollet *et al.* 2005a). More precisely, fitting the data for the pressure along the axis $y=0$ (figure 22) by a power-law yields the following dependence: $P(x) = (9.5 \pm 0.7)x^{-1.13 \pm 0.05}$ (P expressed in Pa and x in cm). The exponent is not very different from the -1 exponent for the stress distribution in an elastic medium under a point-like force (Landau & Lifshitz 1981).

4.2.3. Coupling between statistical elastic strain, velocity gradients and T1s

The asymmetric distribution of the T1s (figure 20) is a major result of this study, since the plastic flow of the foam results from the superposition of many T1s. Since T1s are more likely to occur for deformed bubbles, it is interesting to compare their distribution with the map of statistical elastic strain (figure 13). Such a comparison reveals that the regions of frequent T1s do correspond to high deformation, but the correlation is not simple: for instance, upstream from the obstacle, the deformation is maximal at $x=0$ (figure 14), whereas the T1s are more likely to occur on the sides of the obstacle, not at $x=0$ (figure 21). This is because in this region, the velocity gradients acts to increase the pre-existent deformation (figure 15). There is thus a strong coupling between the statistical elastic strain, the velocity gradients and the T1 distribution, which we will analyse and model in future studies.

4.3. Comparison with force measurements and discussion of the quasi-static regime

We now qualitatively compare our results to the force measurements realized in the same conditions in Dollet *et al.* (2005c). To summarize, that study showed that the drag exerted by a flowing foam on a circular obstacle scales as

$$F = F_0 + \text{const} \times \eta^{0.77 \pm 0.05} v_0, \quad (4.1)$$

with η the bulk viscosity, and F_0 a decreasing function of the bubble area. The independence of the pressure and the bubble deformation of the flow rate (figure 22) is in qualitative agreement with the linear increase of the force exerted by the flowing

foam on the obstacle (Dollet *et al.* 2005c), if we assume that the velocity-dependent contribution to the force is mainly due to the viscous friction in the liquid films between the obstacle and the surrounding bubbles. On the other hand, the exponent for the bulk viscosity in (4.1) is close to 1, but the small difference is significant. This means that increasing the velocity or the bulk viscosity probably does not have strictly the same effect, as would be expected if the force scaled only with a capillary number $Ca = \eta v_0 / \gamma$. But figures 22 and 25 do not enable this small difference between a variation of velocity v_0 and a variation of bulk viscosity to be precisely captured. Concerning the foam thickness, figure 24 shows that the fore–aft differences in pressure and bubble deformation increase with the foam thickness, hence decrease with the fluid fraction. This is compatible with the decrease of the drag with the fluid fraction reported in Raufaste *et al.* (2007). The role of the bubble area is more complex: we showed in §3.3.2 that this parameter does not influence the bubble deformation much, but that the fore–aft difference in pressure decreases with increasing bubble area. The bubble deformation and pressure being the two contributions to the yield drag F_0 in (4.1), this qualitatively agrees with the fact that F_0 decreases with the bubble area. Moreover, the decrease of the amplitude of the pressure variations with increasing bubble area is not rescaled by simple laws involving only bubble area, probably because of the complex three-dimensional shape of the bubble. The last control parameter studied, the obstacle itself, shows that the boundary conditions at the obstacle play no significant role. The size of the obstacle has two influences: the bigger the circle, the higher the velocity at its sides, due to the imposed constriction, and the higher the amplitude of variation of the pressure. This is compatible with the measured values of the drag coefficient (ratio of drag and obstacle radius) reported in Dollet *et al.* (2005c) for these three obstacles: equal for the cogwheel and the big circle, and slightly lower for the small circle.

We can now also confirm that the system remains in a quasi-static regime even at the highest velocity and bulk viscosity. The relaxation time τ_{T1} , introduced in §4.1, is the time needed for the foam to recover local equilibrium after a T1. Therefore, the proportion of time away from equilibrium is $f_{T1}\tau_{T1}$, where f_{T1} is the frequency of T1 per link introduced in §2.2.3 (or, equivalently, f_{T1}^{-1} is the average lifetime of a given link). This proportion remains very small in our range of parameters: f_{T1} does not exceed 0.25 s^{-1} in the reference experiment (figure 20), and its maximal value for the highest flow rate is 0.7 s^{-1} . Conversely, the relaxation time is very short: $\tau_{T1} < 0.1\text{ s}$ as shown in §4.1; furthermore, it has no apparent dependence on the bulk viscosity, which is compatible with the observations of Durand & Stone (2006). Hence, the proportion of time away from equilibrium, $f_{T1}\tau_{T1}$, remains lower than 7%. The transition to a non-quasi-static regime would thus require a much higher velocity, or a larger relaxation time. This is in principle possible with a surfactant with higher surface elasticity and/or viscosity (Durand & Stone 2006), or by adjusting the fluid fraction: for dry foam such as in Hele-Shaw cells, the velocity gradients and hence the friction within the films are large, which slows down the relaxation after a T1. Conversely, for wet foams such as bubble rafts, a T1 mobilizes a large amount of water, which also delays the relaxation. Therefore, the ‘liquid pool’ system, where intermediate fluid fractions are achieved, probably minimizes the relaxation time and promotes quasistatic regimes.

Finally, it is worth noting that the robust quasistatic regime in our experiments does not contradict the fact that the dynamical drag, $F - F_0$ in (4.1), is comparable to the yield drag F_0 and even exceeds it at our higher velocities (Dollet *et al.* 2005c). The dynamical drag arises from the friction induced by the motion of bubbles along

the obstacle. The surfactant used in this study has a low interfacial viscoelasticity: the surface elasticity is $8 \pm 1 \text{ mN m}^{-1}$, and the surface viscosity is $1 \pm 1 \text{ kg s}^{-1}$ (Dollet), hence we can assume that the interfaces are fluid and that the friction is therefore dominated by bulk dissipation in the Plateau borders (Denkov *et al.* 2005). Conversely, the relaxation after a T1 is mainly driven by interfacial viscoelasticity (Durand & Stone 2006). The dynamical drag and the transition from quasistatic to out-of-equilibrium regimes are thus associated with independent sources of dissipation and decoupled, as shown also by Marmottant & Graner (2007), who indeed predict a regime where foam flows can still be quasistatic even though viscous stresses dominate elastic ones.

5. Conclusions

We have performed a systematic local study of the flow of foam around a circular obstacle, quantifying the elasticity by the statistical elastic strain tensor and the pressure field, the plasticity by a tensorial descriptor of bubble rearrangements, and the flow by the velocity field and its gradients. We demonstrate in §3.1 that such a continuous approach is justified and suitable in this case. The study of a reference experiment (§3.2) shows a marked fore–aft asymmetry: the velocity exhibits an overshoot in the wake, and the bubble rearrangements spread more at the leading side than in the wake of the obstacle. This reveals the complex behaviour of the foam, dictated by the coupling between elasticity (bubble deformations), plasticity (bubble rearrangements) and flow (velocity gradients).

We showed in §3.3.1 that the rescaled velocity v/v_0 , the pressure and the bubble deformation do not depend significantly on the flow rate, in the range studied. Hence, the yield and the dynamic contributions in foam rheology seem to be decoupled, which justifies recent approaches to model foam flows (and more generally, complex fluid flows) as Bingham plastics with an added elastic term independent of the shear rate (Takeshi & Sekimoto 2005). In this context, the approach of Janiaud *et al.* (2006) is promising, since it contains the essential ingredients of the two-dimensional rheology of foams: elasticity up to a yield stress, plasticity at high imposed strain, internal viscosity accounting for the motion within the films between bubbles, and external friction (or viscous drag) between the flowing foam and the confining boundaries. However, such scalar viscoelastoplastic approaches are not sufficient in our context, where the complex flow around an obstacle requires a tensorial description. It would be interesting to perform the same experiments at higher flow rate, to determine when this decoupling between elastic and the dynamic contribution breaks down, and to investigate whether phenomena such as elastic turbulence (Groisman & Steinberg 2000) could then occur in the wake of the obstacle.

The detailed results shown in §3, combined with the associated force measurements reported in Dollet *et al.* (2005a), severely constrain the rheological models adapted to describe liquid foams. The foam flowing around an obstacle intrinsically exhibits yield stress and dissipation (yield drag on the obstacle (de Bruyn 2004; Dollet *et al.* 2005c)), and elastic stress (fore–aft asymmetry); all these effects can only be captured by an viscoelastoplastic and tensorial model.

We thank Simon Cox who kindly calculated figure 4(a) and gave us the permission to publish it.

REFERENCES

- ARIGO, M. T. & MCKINLEY, G. H. 1998 An experimental investigation of negative wakes behind spheres settling in a shear-thinning viscoelastic fluid. *Rheol. Acta* **37**, 307–327.
- ASIPAUSKAS, M., AUBOUY, M., GLAZIER, J. A., GRANER, F. & JIANG, Y. 2003 A texture tensor to quantify deformations: The example of two-dimensional flowing foams. *Granular Matt.* **5**, 71–74.
- AUBOUY, M., JIANG, Y., GLAZIER, J. A. & GRANER, F. 2003 A texture tensor to quantify deformations. *Granular Matt.* **5**, 67–70.
- BATCHELOR, G. K. 1970 The stress system in a suspension of force-free particles. *J. Fluid Mech.* **41**, 545–570.
- BEAULNE, M. & MITSOULIS, E. 1997 Creeping motion of a sphere in tubes filled with Herschel–Bulkley fluids. *J. Non-Newtonian Fluid Mech.* **72**, 55–71.
- BRAKKE, K. 1992 The Surface Evolver. *Exp. Maths* **1**, 141–165.
- DE BRUYN, J. R. 2004 Transient and steady-state drag in foam. *Rheol. Acta* **44**, 150–159.
- BUSH, M. B. 1994 On the stagnation flow behind a sphere in a shear-thinning viscoelastic fluid. *J. Non-Newtonian Fluid Mech.* **55**, 229–247.
- BUZZA, D. M. A., LU, C. Y. D. & CATES, M. E. 1995 Linear shear rheology of incompressible foams. *J. Phys. II Paris* **5**, 37–52.
- CANTAT, I. & DELANNAY, R. 2003 Dynamical transition induced by large bubbles in two-dimensional foam flows. *Phys. Rev. E* **67**, 031501.
- CANTAT, I. & DELANNAY, R. 2005 Dissipative flows of two-dimensional foam. *Eur. Phys. J. E* **18**, 55–67.
- CANTAT, I., KERN, N. & DELANNAY, R. 2004 Dissipation in foam flowing through narrow channels. *Europhys. Lett.* **65**, 726–732.
- CANTAT, I. & PITOIS, O. 2005 Mechanical probing of liquid foam ageing. *J. Phys. Condens. Matt.* **17**, S3455–S3461.
- CANTAT, I., POLONI, C. & DELANNAY, R. 2006 Experimental evidence of flow destabilization in a two-dimensional bidisperse foam. *Phys. Rev. E* **73**, 011505.
- CLANCY, R. J., JANIAUD, É., WEAIRE, D. & HUTZLER, S. 2006 The response of two-dimensional foams to continuous applied shear in a Couette rheometer. *Eur. Phys. J. E* **21**, 123–132.
- COHEN-ADDAD, S., HÖHLER, R. & KHIDAS, Y. 2004 Origin of the slow linear viscoelastic response of aqueous foams. *Phys. Rev. Lett.* **93**, 028302.
- COURTY, S., DOLLET, B., ELIAS, F., HEINIG, P. & GRANER, F. 2003 Two-dimensional shear modulus of a Langmuir foam. *Europhys. Lett.* **64**, 709–715.
- COX, S. J., ALONSO, M. D., HUTZLER, S. & WEAIRE, D. 2000 The Stokes experiment in a foam. In *Proc. 3rd Euroconference on Foams, Emulsions and their Applications*. (ed. P. L. J. Zitha, J. Banhard & P. L. M. M. Verbist), pp. 282–289. MIT Verlag, Bremen.
- COX, S. J., VAZ, M. F. & WEAIRE, D. 2003 Topological changes in a two-dimensional cluster. *Eur. Phys. J. E* **11**, 29–35.
- DEBRÉGEAS, G., TABUTEAU, H. & DI MEGLIO, J. M. 2001 Deformation and flow of a two-dimensional foam under continuous shear. *Phys. Rev. Lett.* **87**, 178305.
- DENKOV, N. D., SUBRAMANIAN, V., GUROVICH, D. & LIPS, A. 2005 Wall slip and viscous dissipation in sheared foams: Effect of surface mobility. *Colloid. Surf. A* **263**, 129–145.
- DERJAGUIN, B. 1933 Die elastischen Eigenschaften der Schäume. *Kolloid Z.* **64**, 1–6.
- DOLLET, B. 2005 Écoulements bidimensionnels de mousse autour d'obstacles, PhD thesis, unpublished, available at <http://www-lsp.ujf-grenoble.fr/pdf/theses/dtbn.pdf>.
- DOLLET, B., AUBOUY, M. & GRANER, F. 2005a Anti-inertial lift in foams: A signature of the elasticity of complex fluids. *Phys. Rev. Lett.* **95**, 168303.
- DOLLET, B., DURTH, M. & GRANER, F. 2006 Flow of foam past an elliptical obstacle, *Phys. Rev. E* **73**, 061404.
- DOLLET, B., ELIAS, F., QUILLIET, C., HUILLIER, A., AUBOUY, M. & GRANER, F. 2005b Two-dimensional flows of foam: Drag exerted on circular obstacles and dissipation. *Colloids Surf. A* **263**, 101–110.
- DOLLET, B., ELIAS, F., QUILLIET, C., RAUFASTE, C., AUBOUY, M. & GRANER, F. 2005c Two-dimensional flow of foam around an obstacle: Force measurements. *Phys. Rev. E* **71**, 031403.

- DOU, H. S. & PHAN-THIEN, N. 2003 Negative wake in the uniform flow past a cylinder. *Rheol. Acta* **42**, 383–409.
- DURAND, M. & STONE, H. A. 2006 Relaxation time of the topological T1 process in a two-dimensional foam. *Phys. Rev. Lett.* **97**, 226101.
- DURIAN, D. J. 1997 Bubble-scale model of foam mechanics: Melting, nonlinear behavior, and avalanches. *Phys. Rev. E* **55**, 1739–1751.
- GOPAL, A. D. & DURIAN, D. J. 1999 Shear-induced “melting” of an aqueous foam. *J. Colloid Interface Sci.* **213**, 169–178.
- GOPAL, A. D. & DURIAN, D. J. 2003 Relaxing in foam. *Phys. Rev. Lett.* **91**, 188303.
- GROISMAN, A. & STEINBERG, V. 2000 Elastic turbulence in a polymer solution flow. *Nature* **405**, 53–55.
- GUESLIN, B., TALINI, L., HERZHAFT, B., PEYSSON, Y., ALLAIN, C. 2006 Flow induced by a sphere settling in an aging yield-stress fluid. *Phys. Fluids* **18**, 103101.
- GUYON, É., HULIN, J. P. & PETIT, L. 2001 *Hydrodynamique Physique*. EDP Sciences/CNRS Éditions, Paris.
- HARLEN, O. G. 2002 The negative wake behind a sphere sedimenting through a viscoelastic fluid. *J. Non-Newtonian Fluid Mech.* **108**, 411–430.
- HASSAGER, O. 1979 Negative wake behind bubbles in non-Newtonian fluids. *Nature* **279**, 402–403.
- HÖHLER, R. & COHEN-ADDAD, S. 2005 Rheology of liquid foams *J. Phys. Condens. Matter* **17**, R1041–R1069.
- HÖHLER, R., COHEN-ADDAD, S. & LABIAUSSE, V. 2004 Constitutive equation to describe the nonlinear elastic response of aqueous foams and concentrated emulsions. *J. Rheol.* **48**, 679–690.
- JANIAUD, É. & GRANER, F. 2005 Foam in a two-dimensional Couette shear: A local measurement of bubble deformation. *J. Fluid Mech.* **532**, 243–267.
- JANIAUD, É., WEAIRE, D. & HUTZLER, S. 2006 Two-dimensional foam rheology with viscous drag. *Phys. Rev. Lett.* **97**, 038302.
- KABLA, A. & DEBRÉGEAS, G. 2003 Local stress relaxation and shear-banding in a dry foam under shear. *Phys. Rev. Lett.* **90**, 258303.
- KERN, N., WEAIRE, D., MARTIN, A., HUTZLER, S. & COX, S. J. 2004 Two-dimensional viscous froth model for foam dynamics, *Phys. Rev. E* **70**, 041411.
- KHAN, S. A. & ARMSTRONG, R. C. 1986 Rheology of foams. I. Theory for dry foams. *J. Non-Newtonian Fluid Mech.* **22**, 1–22.
- KHAN, S. A. & PRUD'HOMME, R. 1996 *Foams*, Dekker.
- KIM, J. M., KIM, C., CHUNG, C., AHN, K. H. & LEE, S. J. 2005 Negative wake generation of FENE–CR fluids in uniform and Poiseuille flow past a cylinder. *Rheol. Acta* **44**, 600–613.
- KRAYNIK, A. M. 1988 Foam flows. *Annu. Rev. Fluid Mech.* **20**, 325–357.
- LANDAU, L. D. & LIFSHITZ, E. M. 1981 *Theory of Elasticity*, 2nd edn. Pergamon.
- LANGER, S. A. & LIU, A. J. 1997 Effect of random packing on stress relaxation in foam. *J. Phys. Chem. B* **101**, 8667–8671.
- LARSON, R. G. 1999 *The Structure and Rheology of Complex Fluids*. Oxford University Press.
- LAURIDSEN, J., TWARDOS, M. & DENNIN, M. 2002 Shear-induced stress relaxation in a two-dimensional wet foam. *Phys. Rev. Lett.* **89**, 098303.
- LAURIDSEN, J., CHANAN, G. & DENNIN, M. 2004 Velocity profiles in slowly sheared bubble rafts. *Phys. Rev. Lett.* **93**, 018303.
- MARMOTTANT, P. & GRANER, F. 2007 A quasistatic model for an elastic, plastic, viscous foam. *Eur. Phys. J. B.* (submitted).
- MASON, T. G., BIBETTE, J. & WEITZ, D. A. 1995 Elasticity of compressed emulsions. *Phys. Rev. Lett.* **75**, 2051–2054.
- MASON, T. G., BIBETTE, J. & WEITZ, D. A. 1996 Yielding and flow of monodisperse emulsions. *J. Colloid Interface Sci.* **179**, 439–448.
- MITSOULIS, E. 2004 On creeping drag flow of a viscoplastic fluid past a circular cylinder: Wall effects. *Chem. Engng Sci.* **59**, 789–800.
- PICARD, G., ADJARI, A., LEQUEUX, F. & BOCQUET, L. 2004 Elastic consequences of a single plastic event: A step towards the microscopic modeling of the flow of yield stress fluid. *Eur. Phys. J. E* **15**, 371–381.

- PRAATT, E. & DENNIN, M. 2003 Nonlinear stress and fluctuation dynamics of sheared disordered wet foam *Phys. Rev. E* **67**, 054102.
- PRINCEN, H. M. 1983 Rheology of foams and highly concentrated emulsions. I. Elastic properties and yield stress of a cylindrical model system. *J. Colloid Interface Sci.* **91**, 160–175.
- PRINCEN, H. M. 1985 Rheology of foams and highly concentrated emulsions. II. Experimental study of the yield stress and wall effects for concentrated oil-in-water emulsions. *J. Colloid Interface. Sci.* **105**, 150–171.
- RAUFASTE, C., DOLLET, B., COX, S. J., GRANER, F. & JIANG, Y. 2007 Yield drag in a two-dimensional foam around a circular obstacle: Effect of fluid fraction. *Eur. Phys. J. E* (to appear).
- ROQUET, N. & SARAMITO, P. 2003 An adaptive finite element method for Bingham fluid flows around a cylinder *Comput. Methods Appl. Mech. Engng* **192**, 3317–3341.
- SAINT-JALMES, A. & DURIAN, D. J. 1999 Vanishing elasticity for wet foams: Equivalence with emulsions and role of polydispersity. *J. Rheol.* **43**, 1411–1422.
- SOLLICH, P., LEQUEUX, F., HÉBRAUD, P. & CATES, M. E. 1997 Rheology of soft glassy materials. *Phys. Rev. Lett.* **78**, 2020–2023.
- STAMENOVIĆ, D. & WILSON, T. A. 1984 The shear modulus of liquid foam. *J. Appl. Mech.* **51**, 229–231.
- TAKESHI, O. & SEKIMOTO, K. 2005 Internal stress in a model elastoplastic fluid. *Phys. Rev. Lett.* **95**, 108301.
- VAZ, M. F. & COX, S. J. 2005 Two-bubble instabilities in quasi-two-dimensional foams. *Phil. Mag. Lett.* **85**, 415–425.
- WANG, Y., KRISHAN, K. & DENNIN, M. 2006 Impact of boundaries on velocity profiles in bubble rafts. *Phys. Rev. E* **73**, 031401.
- WEAIRE, D. & HUTZLER, S. 1999 *The Physics of Foams*. Oxford University Press.